Factors contributing to deep slab dip angles in reconstructions of past mantle flow

Joshua Weber[1] and Nicolas Flament[1*]

[1]School of Earth, Atmospheric and Life Sciences, University of Wollongong, Northfields Avenue, NSW 2522, Australia

*Corresponding author; e-mail address: nflament@uow.edu.au

Key points

- We compare deep slab dip angles in mantle flow and tomographic models
- Trench retreat, convective vigour and mantle viscosity influence deep slab dip angle
- Our comparison indicates where global tectonic reconstructions could be improved

Abstract

Individual sinking slabs present markedly different dip angles between 410 km and 660 km depths, from vertical slabs penetrating the lower mantle to slabs stagnating above the lower mantle. Proposed factors determining these contrasted deep slab dip angles include the magnitude and evolution of trench retreat, mantle viscosity, slab rheology and phase changes. Here we assess the success of paleo-geographically driven global mantle flow models in matching slabs in tomographic models down to 1,000 km depth. We quantify the spatial match between predicted present-day mantle temperature anomalies and vote maps of tomographic models. We investigate the sensitivity of the spatial match to input parameters of the mantle flow model: imposed tectonic reconstruction, model start age, Rayleigh number, viscosity contrast between the upper and lower mantle, and phase changes. We evaluate the visual match between model slabs and tomographic vote maps for three circum-Pacific regions with contrasted deep slab dip angles. The match between predicted model slabs and slabs inferred

from tomography can be used to calibrate the Rayleigh number and viscosity contrast between the upper and lower mantle appropriate for our models. The temporal evolution of the models and the global match at present-day suggest that the subduction history could be refined in the global tectonic reconstructions that we considered. For example, subduction to the east of Japan should be offset by approximately 100 km to the west at ~ 80 Ma to match the anchoring of the plate into the lower mantle suggested by tomography.

Keywords: mantle convection; tectonic reconstructions; tomography; subduction; slab

Plain Language Summary

Oceanic lithosphere is recycled as sinking slabs into Earth's mantle, and the analysis of global earthquake data compiled in tomographic models has revealed that the dip angle of slabs varies between regions. In this manuscript, we analyse the geometry of upper mantle slabs predicted by forward models of past global mantle flow that follow imposed surface tectonic motions. We present some of the first quantifications of the spatial match between the present-day mantle temperature predicted by reconstructions of past global mantle flow and that imaged by global tomographic models. Few studies have quantified this match and clearly exposed it spatially. We quantify the match between the upper mantle slabs predicted by these models and that inferred from a series of tomographic models. We show that the models successfully reproduce the steeply dipping Mariana slab and stagnating Western Pacific slab under Japan and the intermediate geometry of the Farallon and Nazca slab under South America, and we find that trench retreat is the main driver of the geometry of these slabs. Our results suggest that the geometry of slabs can be used to refine global tectonic reconstructions and to calibrate the Rayleigh number and viscosity contrast between upper and lower mantle in global mantle flow models.

Introduction

Global tomographic models have revealed fast velocity anomalies that are interpreted as subducted slabs (oceanic lithosphere that has sunk into Earth's mantle) and that present varying dip angles in the transition zone (between 410 km and 660 km depth) and across the upper-

lower mantle boundary (from 660 km depth) (van der Hilst and Mann, 1994; Fukao et al., 2001; Ren et al., 2007; Li et al., 2008; Van der Meer et al., 2018). At these depths, the two most contrasted slab dip angles are slabs penetrating vertically into the lower mantle (such as the Mariana slab) and slabs flattening out in the transition zone (such as the Western Pacific slab) (Van der Hilst et al., 1997; Ren et al., 2007; Běhounková and Čížková, 2008; Li et al., 2008; Goes et al., 2017; Wu et al., 2022). For example, slabs at the Mariana Trench or underneath Peru are steeply dipping through the transition zone sink into the lower mantle, whereas slabs in the Izu-Bonin region or the Western Pacific plate under Japan are more gently dipping through the transition zone and lie flat at the upper-lower mantle boundary (Fukao and Obayashi, 2013; Wu et al., 2022).

Several factors have been proposed to explain the origin of these variations in the dip angles of slabs in the transition zone, which is sometimes referred to as the 'deep slab dip angles' (e.g., Schellart, 2007). These factors include the temporal evolution of the magnitude of trench migration occurring at the surface (van der Hilst and Seno, 1993; Griffiths et al., 1995; Guillou-Frottier et al., 1995; Christensen, 1996; Olbertz et al., 1997; Goes et al., 2017), the viscosity and rheology of the mantle (Hager and Richards, 1989; Peltier, 1996; Čižková and Čadek, 1997; Kido and Čadek, 1997; Čížková et al., 2002; Běhounková and Čížková, 2008; Garel et al., 2014; Mao and Zhong, 2018) and the presence of phase changes (Irifune and Ringwood, 1993; Agrusta et al., 2017; Goes et al., 2017) at around 410 km and 660 km depths. Geodynamic models have also revealed that deep slab dip angles change over time, evolving and developing as part of the convecting mantle (e.g., Agrusta et al., 2017).

Because of their computational cost, investigations of the dynamics of slabs and of their interaction with the mantle transition zone are often carried out in two-dimensions (Čižková and Čadek, 1997; Olbertz et al., 1997; Čížková et al., 2002; Garel et al., 2014; Honda, 2016; Agrusta et al., 2017; Čížková and Bina, 2019; Yang et al., 2019), and the present-day slabs

predicted by such dynamically-consistent models are compared to first-order with slabs imaged by tomographic models to the first order. A distinct approach consists of comparing the present-day slab locations predicted by tectonically-driven three-dimensional mantle flow models with that imaged by global seismic tomography models (Becker and Boschi, 2002; Zahirovic et al., 2016; Coltice and Shephard, 2018; Hu et al., 2018; Mao and Zhong, 2018; Peng et al., 2021). Such comparisons are usually visual or consist of global correlations that do not preserve spatial information (Becker and Boschi, 2002), although finer quantitative comparisons are emerging (Flament, 2019; Peng and Liu, 2023).

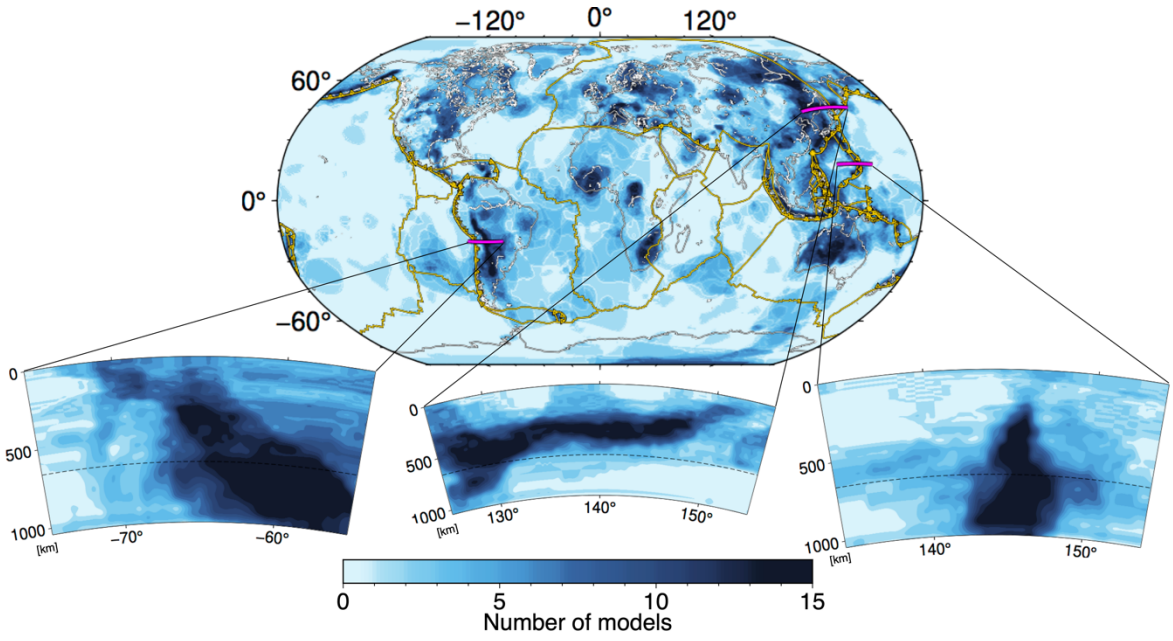

Figure 1. Vote maps for global P-wave tomographic models at 660 km depth and cross-sections down to 1000 km depth for South America, Japan and the Mariana Trench, from left to right. These locations have been selected to show some of the variability in the deep slab dip angles imaged by seismic tomography models. On the maps, golden lines represent plate boundaries (subduction zone polarities are indicated by triangles on the overriding plates), white lines represent coastlines and transects are shown in magenta. On the cross-sections, the dashed line indicated the upper-lower mantle boundary at 660 km depth.

In this study, we quantitively compare the location of present-day slabs predicted by tectonically-driven three-dimensional mantle flow models with that imaged by global seismic

tomography models between 400 km and 1000 km depth, a depth range that captures the transition zone and the uppermost lower mantle. Because seismic tomography models are based on different data and methods (e.g., Becker and Boschi, 2002; Romanowicz, 2008; Hosseini et al., 2018), we use an approach that combines them into vote maps that reveal similarities and differences in global seismic velocity models (Shephard et al., 2017). We visually evaluate the deep dip angle of slabs predicted by forward time-dependent global mantle flow models, and for the present-day compare it to vote maps of tomographic models under the Mariana Trench, the Bolivian orocline in South America, and under Japan (Fig. 1). To ascertain whether deep slab dip angle is driven by surface plate motions or by mantle parameters of the flow models, we vary the tectonic reconstruction used as input for mantle flow models, as well as the vigour of mantle convection, the presence of phase changes, and mantle viscosity. Our approach makes it possible to highlight first-order differences between slabs in mantle flow models and in tomographic models, and to recommend modifications to global tectonic reconstructions.

1. Methods

2.1. Paleogeographically constrained mantle flow models

We consider global mantle flow models that take tectonic reconstruction as surface boundary condition to reconstruct the structure of Earth's mantle over time (Bower et al., 2015), and we map model slabs from cold temperature anomalies.

2.1.1 Set-up of forward reconstructions of past mantle convection

We use *CitcomS*, in which the mantle is a shell represented with finite-elements in spherical geometry. We obtain an average resolution of ~50 × 50 × 15 km at the surface, ~40 × 40 ×

100 km in the mid-mantle, and ~28 × 28 × 27 km at the core-mantle boundary (CMB) by using 129 × 129 × 65 × 12 ≈ 13 million elements and refining the mesh vertically towards the surface and the core-mantle boundary. The thermal structure of the lithosphere and of the thermal structure of slabs down to 350 km are built using the half-space cooling model from global maps of the age of the lithosphere (computed from the reconstruction as in Williams et al., 2021) and from the location and polarity of subduction zones obtained from the tectonic reconstructions. The initial condition consists at age a_0 (Table 1) of an adiabat between two thermal boundary layers and of slabs inserted down to z_0 (Table 1) with a dip of 45º down to 425 km and a dip of 90º below 425 km depth. Plate velocities are imposed in one-million-year intervals, and the thermal structure of the lithosphere (down to the base of the lithosphere) and of slabs (down to 350 km depth), computed in one-million-year increments using a diffusive cooling model, are blended in with the dynamic solution at each time step (Bower et al., 2015). This approach makes it possible to obtain one-sided subduction in time-dependent global mantle convection models with computationally affordable resolution and viscosity variations.

2.1.2 Mantle parameters varied across forward reconstructions of past mantle convection

Phase changes. We consider the effect of phase changes at 410 km depth and 660 km depth and assume that both phase changes occur over a 40 km depth range. At 410 km depth, we assume a density change of 3% and a Clapeyron slope equal to 4 MPa K^{-1} (Billen, 2008, and references therein). At 660 km depth, we assume a density change of 7% and a Clapeyron slope equal to -2 MPa K^{-1} (Billen, 2008, and references therein). Case C1 includes phase changes at 410 km and 660 km depth and case C2 includes a phase change at 660 km depth.

Viscosity contrast between the upper and lower mantle. Viscosity varies with depth, composition, temperature and pressure following $\eta = \eta(r)\,\eta_0\,\exp\left\{\frac{[E_\eta+\rho_0 g Z_\eta(R_0-r)]}{[R(T+T_{off})]}-\frac{[E_\eta+Z_\eta(R_0-R_c)]}{[R(T_{\mathrm{CMB}}+T_{off})]}\right\}$, where $\eta(r)$ is a pre-factor that is defined for four layers: above 160 km depth, between 160–310 km depth, between 310–660 km depth and below 660 km depth, η_0 is the reference viscosity, r is the radius, R_C = 3,504 km is the radius of the core, E_η = 275 kJ mol^{-1} is the activation energy, $Z_\eta = 2.1 \times 10^{-6}$ m^3 mol^{-1} is the activation volume, R = 8.31 J mol^{-1} K^{-1} is the universal gas constant, T is the dimensional temperature, T_{off} = 452 K is a temperature offset and T_{CMB} = 3380 K is the temperature at the core-mantle boundary. The viscosity pre-factor, activation energy, activation volume and temperature offset were selected to obtain variations in viscosity over three orders of magnitude (viscosity variations were limited to the range 1.1×10^{20} Pa s - 2.2×10^{23} Pa s) across the range of temperatures and pressures. In all cases except C4, the viscosity pre-factor was ten times greater in the lower mantle than in the upper mantle, because such an increase has been proposed to be required to match the geoid in instantaneous mantle flow models (Hager et al., 1985; Ricard et al., 1993). While this increase is at the lower end of the proposed range (by a factor between 10 and 30; Hager et al., 1985), viscosity also increases with pressure in our models, and the preferred viscosity structure (Fig. 2) is generally consistent with independent models matching the geoid (Steinberger and Calderwood, 2006). Because the viscosity structure of the mantle remains poorly constrained (King, 2016), and because the deep slab dip angles depends on viscosity (Garel et al., 2014), we consider a case without increase at 660 km depth (case C4, Fig. 2).

Rayleigh number. We consider the extended-Boussinesq approximation, which accounts for viscous dissipation, an adiabatic temperature gradient, internal heating and a decrease in the coefficient of thermal expansion by a factor of two over the thickness of the mantle

(Chopelas and Boehler, 1992). Convective vigour is determined by the Rayleigh number $Ra = (\alpha_0 \rho_0 g_0 \Delta T h_M^3)/(\kappa_0 \eta_0)$ with $\alpha_0 = 3 \times 10^{-5}$ K^{-1} the coefficient of thermal expansion, $\rho_0 = 4000$ kg m^{-3} the density, $g_0 = 9.81$ m s^{-2} the gravitational acceleration, $\Delta T = 3100$ K the temperature change across the mantle, $h_M = 2{,}867$ km the thickness of the mantle, $\kappa_0 = 1 \times 10^{-6}$ m^2 s^{-1} the thermal diffusivity and $\eta_0 = 1.1 \times 10^{21}$ Pa s the viscosity, and the subscript "0" indicates reference values. With the values listed above, $Ra = 8.60 \times 10^8$. The Rayleigh number (Ra) is increased in increments of an order of magnitude between 8.60×10^6 and 8.60×10^9 across model cases C5-C8 (Table 1). The dissipation number that controls shear heating is $Di = (\alpha_0 g_0 R_0)/C_{p_0}$; with $R_0 = 6{,}371$ km the radius of Earth and $C_{p_0} = 1200$ J kg^{-1} K^{-1} the heat capacity, $Di = 1.56$.

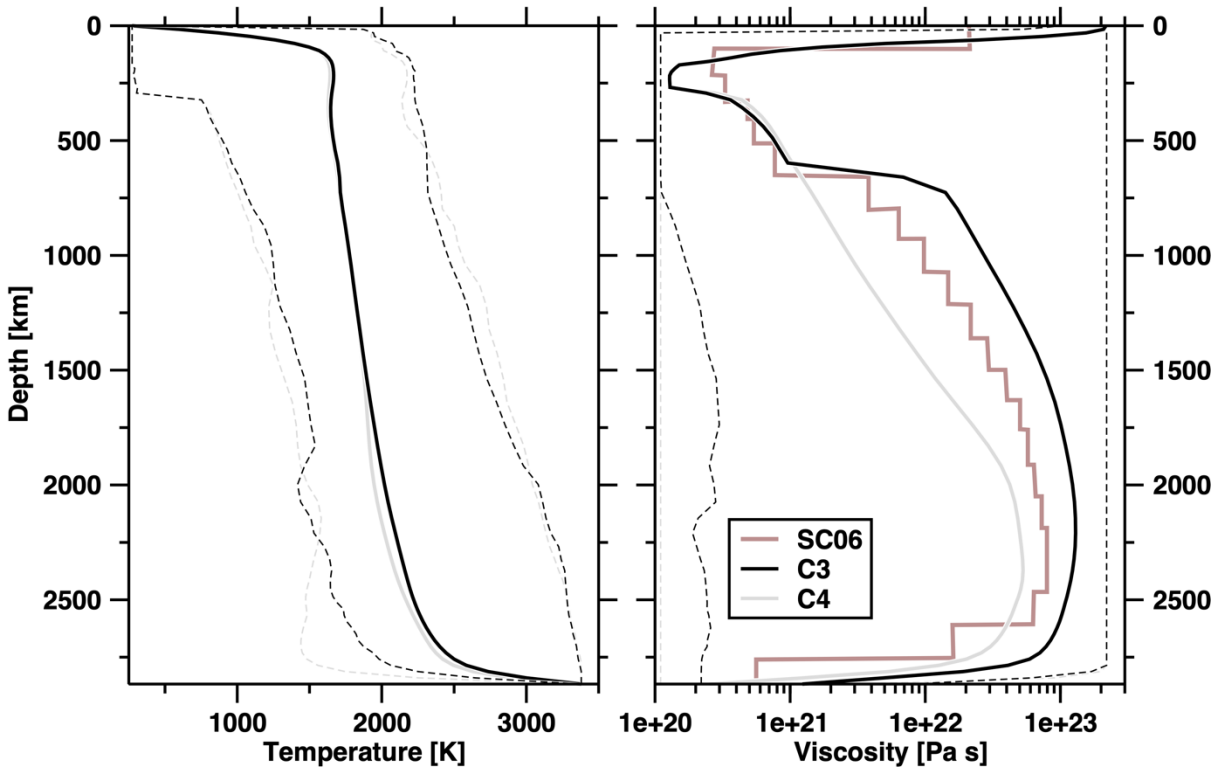

Figure 2. Variations of temperature (left) and viscosity (right) with depth predicted for the present-day for cases C3 (with a viscosity contrast at 660 km depth) and C4 (without viscosity contrast at 660 km depth). Solid lines show the horizontal average and dashed lines show the minimum and maximum. 'SC06' is a viscosity model from Steinberger and Calderwood (2006) calibrated to fit the present-day geoid.

193 *Tectonic reconstructions.* We vary the model start age a_0 and the tectonic reconstruction
194 across a series of model cases. We consider the tectonic reconstructions of Müller et al. (2016),
195 hereafter referred to as Mu16, Matthews et al. (2016), hereafter referred to as Ma16, Young et
196 al. (2019), hereafter referred to as Y19, and Merdith et al. (2021), hereafter referred to as Me21.
197 Reconstruction Mu16 was used for case C9 (a_0 = 230 Ma); it extends back to 230 Ma and uses
198 the reference frames of Steinberger and Torsvik (2008) between 200-100 Ma and of Torsvik
199 et al. (2008) for the last 100 Myr. Reconstruction Ma16 was used for case C5-C8, C11 (a_0 =
200 100 Ma) and C12 (a_0 = 230 Ma) and C11; it is similar to reconstruction Mu16 for the last 230
201 Ma, although it uses the reference frame of Torsvik et al. (2012); for the period 410-230 Ma,
202 it is based on the reconstruction of Domeier and Torsvik (2014). Reconstruction Y19 was used
203 for case C10 (a_0 = 410 Ma); it is based on Ma16 with modifications to decrease global tectonic
204 speeds and trench migration rates, including changes to relative plate motions (closure of the
205 Rheic Ocean and motion of circum-Paleo-Tethys blocks) and using the reference frame of
206 Torsvik and Voo (2002). Reconstruction M21 was used in case C1-C3 (a_0 = 1000 Ma); it links
207 the reconstruction of Merdith et al. (2017) for the period 1000-500 Ma, to the reconstructions
208 of Domeier (2016) and Domeier (2018) for the period 500-410 Ma and to reconstruction Y19
209 for the last 410 Myr. Reconstruction M21 includes the correction to the mantle reference frame
210 suggested by Torsvik et al. (2019) for Panthalassa. We modified the original reference frame
211 of reconstruction M21 that is based on paleomagnetic data by removing the wholesale motion
212 of the lithosphere with respect to the mantle, known as net lithospheric rotation, because
213 imposing lithospheric net rotation induces wholesale motion of the mantle (Rudolph and
214 Zhong, 2014) whereas such motions should dynamically arise from lateral viscosity variations
215 (Ricard et al., 1991).

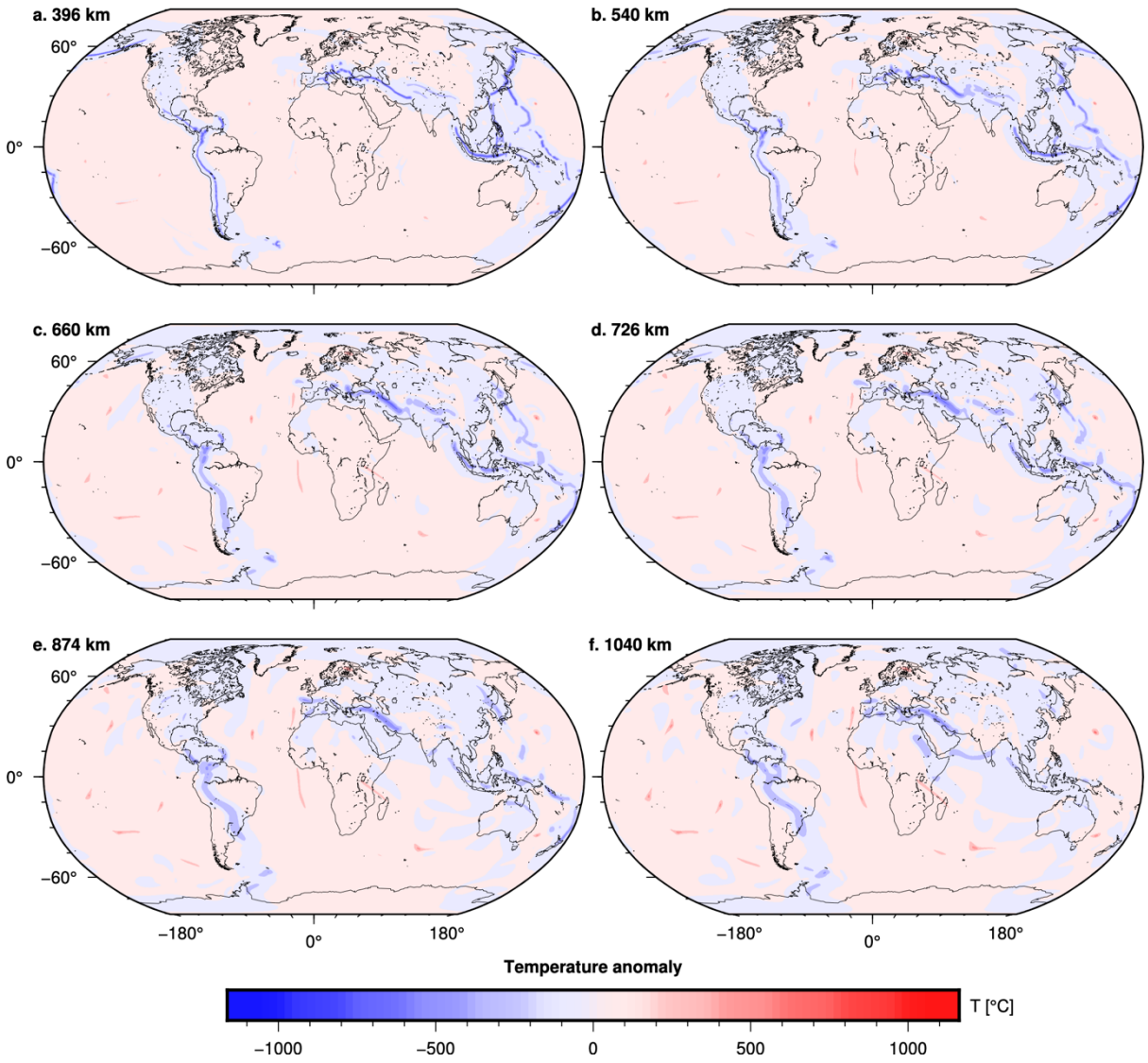

Figure 3. Present-day temperature anomalies defined as deviations from the horizontal average of temperature such as shown in Figure 2, for selected depths and for case C10 (reconstruction Y19, start age 410 Ma). Coastlines are shown in black.

Most of these models have previously been reported in publications: cases C1, C2 and C3 were cases C22, C21 and C20 in Flament et al. (2022), respectively, and cases C5, C6, C7, C8, C9 and C12 were cases C11, C12, C1, C13, C4 and C6 in Flament (2019).

These reconstructions of past mantle flow predict present-day mantle temperature (Fig. 3) from which slabs can be inferred. Overall, the varied parameters make it possible to separately investigate the effect on deep slab dip angle of initial and surface boundary

conditions (tectonic reconstruction and start age) and of parameters affecting mantle convection (Rayleigh number, viscosity structure, phase changes).

Case	Reconstruction	Start Age (Ma)	Rayleigh Number	Viscosity structure	Phase change
			Phase change		
C1	M21	1000	8.60×10^8	0.02,0.002,0.02,0.2	410, 670
C2	M21	1000	8.60×10^8	0.02,0.002,0.02,0.2	670
C3	M21	1000	8.60×10^8	0.02,0.002,0.02,0.2	-
			Viscosity contrast		
C4	M21	1000	8.60×10^8	0.02,0.002,0.02,0.02	-
			Rayleigh number		
C5	Ma16	230	8.60×10^6	0.02,0.02,0.02,0.1	-
C6	Ma16	230	8.60×10^7	0.02,0.02,0.02,0.1	-
C7	Ma16	230	8.60×10^8	0.02,0.02,0.02,0.1	-
C8	Ma16	230	8.60×10^9	0.02,0.02,0.02,0.1	-
			Tectonic reconstruction		
C9	Mu16	230	8.60×10^8	0.02,0.02,0.02,0.02	-
C10	Y19	410	8.60×10^8	0.02,0.002,0.02,0.2	-
C11	Ma16	100	8.60×10^8	0.02,0.002,0.02,0.2	-
C12	Ma16	230	8.60×10^8	0.02,0.002,0.02,0.2	-

Table 1. List of paleogeographically constrained mantle flow models grouped by input parameters.

2.2. Slabs imaged by vote maps of seismic tomographic models

Seismic tomography is one of the main techniques to image Earth's mantle. Regions in which P- and/or S-waves travel faster than a reference model such as PREM (Dziewonski and Anderson, 1981) are inferred to be colder than ambient mantle and to represent slab material that has sunk into the mantle. Seismic tomographic models differ in the data and methods used (Becker and Boschi, 2002; Romanowicz, 2008; Hosseini et al., 2018); for example, S-wave models tend to achieve better coverage of the mantle than P-wave models, although at lower resolution (Grand, 2002). A way to jointly analyse distinct tomographic models is to create 'vote maps' that contour and stack seismic velocity anomalies from different tomographic

models, either by analysing models over a given depth range using cluster analysis (Lekic et al., 2012), or by analysing models at discrete depths (Shephard et al., 2017; Shephard et al., 2021). Here we follow the latter approach to preserve the location of slabs as a function of depth. In the process, areas in which seismic velocity anomalies are greater than the mean of the positive values are attributed a value of one, whereas other areas are given a value of zero; global maps for selected tomographic models are then added together for a given depth (Shephard et al., 2017). The resulting vote maps depend on the number of selected models, and do not add any features that were not present in the underlying tomographic models. The resulting vote maps reveal where tomographic models agree on the presence of fast seismic anomalies, interpreted as slabs. Greater vote counts indicate features that are common across the selected models, whereas lower vote counts indicate features that are only present in fewer models; however, low vote counts do not indicate that features do not exist. Here we created vote maps (e.g., Fig. 8) from the SubMachine website (Hosseini et al., 2018; Hosseini, 2018), focusing on global tomographic models and ignoring models restricted either regionally or in depth. We selected deviations from the mean for fast velocity anomalies down to 1000 km depth for the following global tomographic models:

- 15 P-wave tomographic models: DETOX-P1, DETOX-P2, DETOX-P3 (Hosseini et al., 2020), GAP-P4 (Obayashi et al., 2013), GyPSuM-P (Simmons et al., 2010), HMSL-P06 (Houser et al., 2008), LLNL_G3Dv3 (Simmons et al., 2012), MITP08 (Li et al., 2008), MITP_USA_2011MAR (Burdick et al., 2012), MITP_USA_2016MAY (Burdick et al., 2017), PRI-P05 (Montelli et al., 2006), SP12RTS-P (Koelemeijer et al., 2016), SPani-P (Tesoniero et al., 2015), UU-P07 (Amaru, 2007), TX2019slab-P (Lu et al., 2019)
- and 18 S-wave tomographic models: GyPSuM-S (Simmons et al., 2010), HMSL-S06 (Houser et al., 2008), PRI-S05 (Montelli et al., 2006), S20RTS (Ritsema et al., 1999),

S362ANI+M (Moulik and Ekström, 2014), S40RTS (Ritsema et al., 2011), Savani (Auer et al., 2014), SAW642ANb (Panning et al., 2010), SEISGLOB1 (Durand et al., 2016), SEISGLOB2 (Durand et al., 2017), SEMUCB-WM1 (French and Romanowicz, 2014), SEMum (Lekić and Romanowicz, 2011), SGLOBE-rani (Chang et al., 2015), SP12RTS-S (Koelemeijer et al., 2016), SPani-S (Tesoniero et al., 2015), TX2011 (Grand, 2002), TX2015 (Lu and Grand, 2016), TX2019slab-S (Lu et al., 2019).

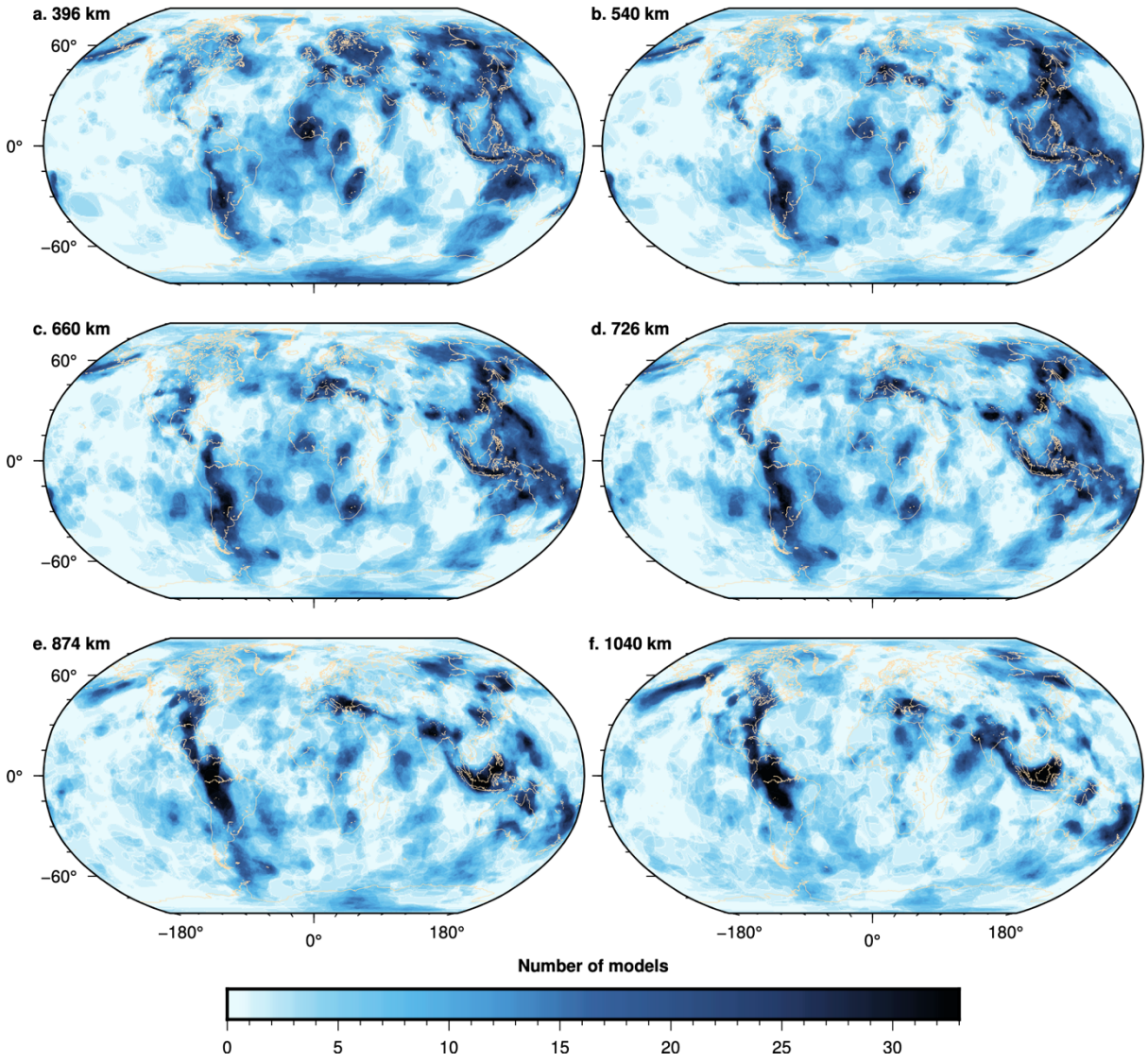

Figure 4. Vote maps for 33 global P- and S-wave tomographic models shown at selected depths. Coastlines are coloured in gold.

2.3 Comparing slabs in mantle flow models and in tomographic models

The considered mantle flow models are not directly based on tomographic models, which makes it possible to compare the temperature structure predicted for the present day to tomographic models. Specifically, we aim to compare the location and deep slab dip angle of predicted cold mantle structures to that of fast seismic anomalies summarised in vote maps from tomographic models. We achieve this comparison by selecting threshold values for predicted temperature anomalies and vote maps of tomographic models. In carrying out this comparison, we keep in mind that tomographic models have been used to regionally refine the global tectonic reconstructions that we use (e.g., Zahirovic et al., 2016). While the initial temperature structure of our forward mantle flow models is derived from tectonic reconstructions rather than from tomographic models, the reconstructions that we use have been informed by tomographic models in some regions for the last ~150-200 Myr, assuming that slabs sink vertically at uniform sinking rates (e.g., Zahirovic et al., 2016).

2.3.1 Selecting thresholds to obtain similar slab cross-sectional areas

To visually and quantitatively compare the spatial match between present-day slabs predicted by mantle flow models and imaged by tomographic models, it is important to ensure that the area of slabs is similar in both types of models. We investigate the area covered by slabs in map view at a given depth for a given threshold of temperature anomalies and vote map, following Flament (2019). We first consider mantle 2% colder than ambient and 7 votes out of 15 P-wave tomographic models (as in Flament, 2019), 11 votes out of 18 S-wave tomographic models and 17 votes out of 33 P- and S-wave tomographic models. These thresholds lead to slabs covering 5-10% of the surface between 400 km and 1000 km depth (Fig. 5a) in tomographic models, and while some flow models fall within that range, the fractional area reaches up to 22% of the surface in case C3. Considering mantle 5% colder than

ambient, 13 votes out of 15 P-wave tomographic models, 14 votes out of 18 S-wave tomographic models and 23 votes out of 33 P- and S-wave tomographic models decreases the slab area to between ~1.5% and 6% and results in a better match between mantle flow and tomographic models (Fig. 5b). We therefore use these latter thresholds in the following.

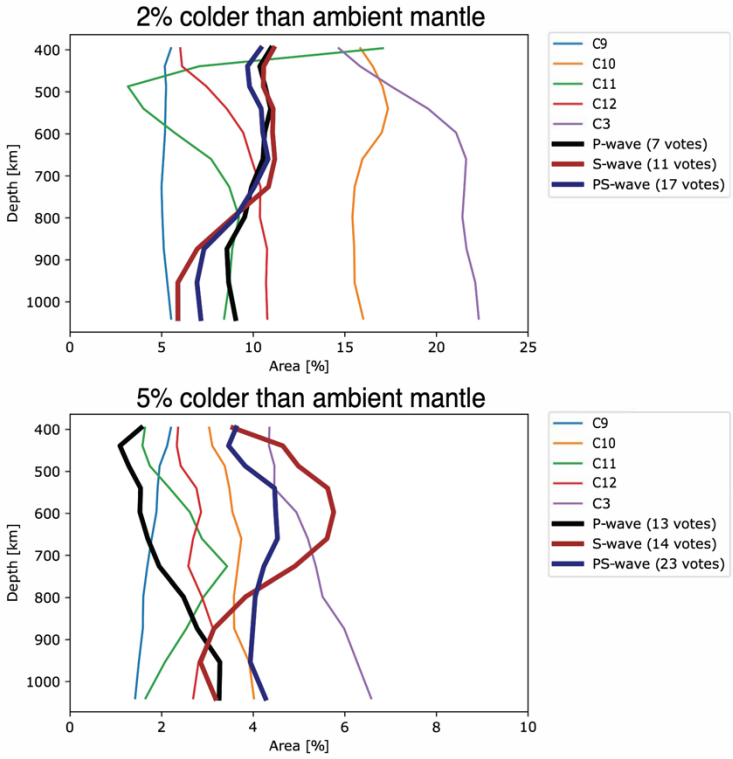

Figure 5. Global slab area as a function of depth for different thresholds in mantle flow models (defined as either 2% and 5% colder than ambient mantle) and tomographic vote maps (defined by the number of votes indicated in the legend out of 15 for P-wave models, 18 for S-waves models, and 33 for P- and S-wave models).

2.3.2. Quantitative spatial match between mantle flow and tomographic models

Visual comparison between mantle flow models and tomographic models reveals the spatial match between predicted present-day mantle temperatures and imaged seismic anomalies between 400 km depth and 1,000 km depth (Fig. 2).

We quantify the present-day match for slabs predicted by mantle flow models and imaged by vote maps of tomographic models. We use two quantities: 1/ the accuracy

319 *Acc* = (*TP* + *TN*)/*A* which measures the ratio of the sum of true positive areas (*TP*) and true
320 negative areas (*TN*) over the entire area (*A*) – this score is relatively large (Fig. 7) because *TN*
321 is large (Fig. 6); and 2/ the sensitivity *S* = *TP*/(*TP*+*FN*) which measures the ratio of *TP* over
322 the sum of *TP* and false negative areas (*FN*) that represents the target area (mantle imaged to
323 be seismically fast) – this score is relatively low (Fig. 7), reflecting that the target area (blue
324 and orange in Fig. 6) is small (of the order of 4% of the total area, Fig. 5b).

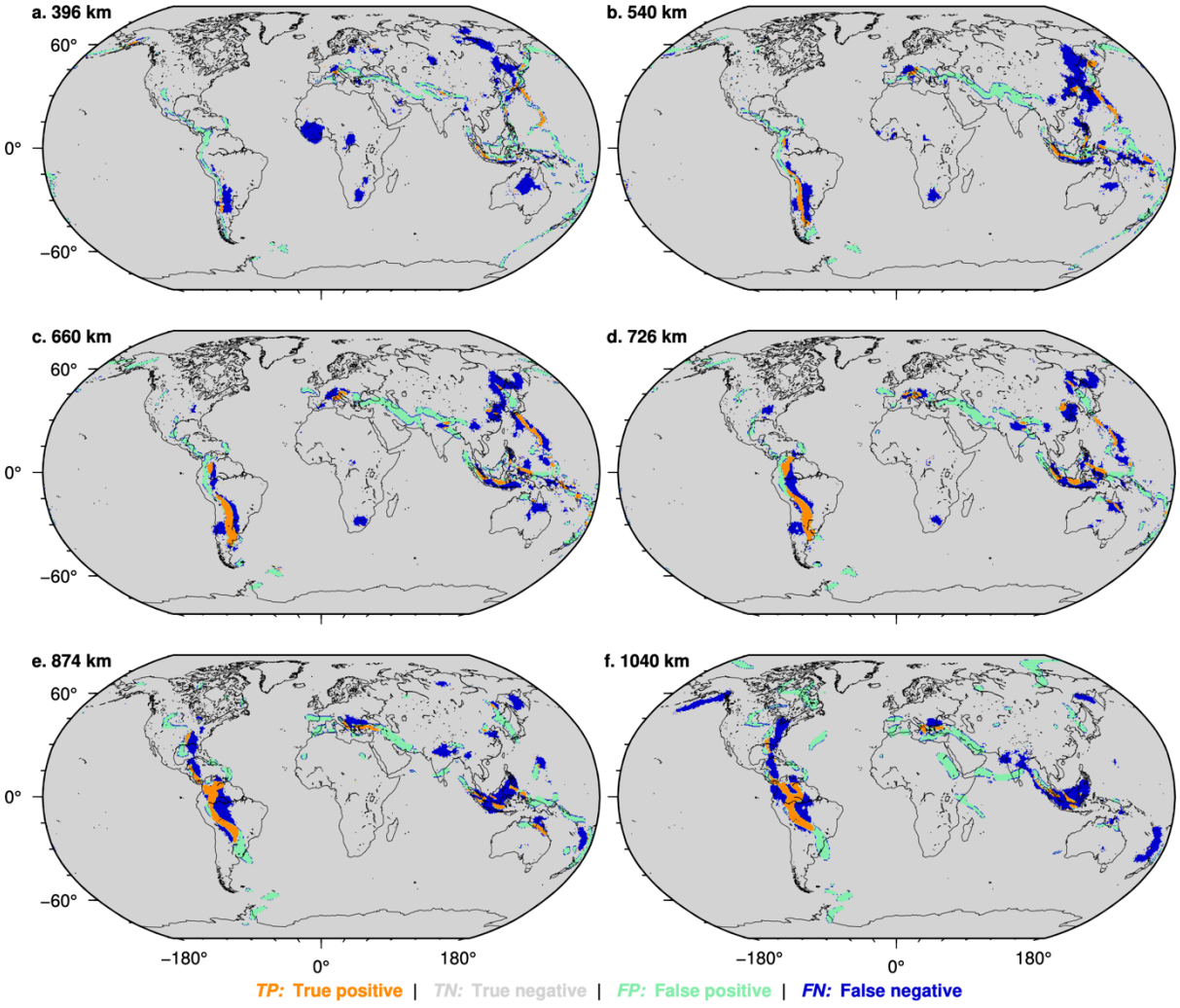

325

326 **Figure 6.** Spatial match between predicted cold lower-mantle and fast seismic anomalies in
327 tomographic models. True positive *TP* areas (in orange) indicate predicted cold mantle and
328 imaged seismically fast mantle, true negative *TN* areas (in grey) indicate that mantle is not
329 predicted to be cold and imaged to be seismically fast, false positive *FP* areas (in green)
330 indicate mantle predicted to be cold but imaged not to be fast, and false negative *FN* areas (in
331 blue) indicate mantle not predicted to be cold but imaged to be fast. Present-day coastlines are
332 shown in black. Results are shown at indicated depths for case C10, mantle 5% colder than
333 ambient and 23 to 33 votes in the combined P- and S-wave vote map of fast seismic anomalies
334 (Shephard et al. 2017).

To further investigate the sensitivity of the spatial match between predicted and imaged slabs, we jointly analyse cross-sections of mantle temperature and vote maps of tomographic models for three locations (Figs 8-10): the Mariana Trench characterised by a steeply dipping slabs that penetrates into the lower mantle (Jaxybulatov et al., 2013; Yang et al., 2019), the Farallon and Nazca plates under the Bolivian orocline of South America as another location featuring a slab that penetrates the lower mantle, although at a lower angle relative to the Mariana (Goes et al., 2008), and the Western Pacific plate characterised by a stagnating slab that lies along the boundary of the upper-lower mantle discontinuity (Li et al., 2008; Honda, 2016; Van der Meer et al., 2018). For each location, we investigate the sensitivity of predicted deep slab dip angles to specific input parameters.

2.4. Temporal evolution of predicted mantle slabs along selected cross-sections

Reconstructions of past mantle flow that best match tomography were selected to be analysed through time at three locations: the Mariana Trench back to 40 Ma or 50 Ma, the Bolivian orocline of South America and under Japan back to 80 Ma. The purpose of this analysis is to investigate the evolution of deep slab dip angles through time, as well as the sensitivity of the evolution of model deep slab dip angle to the input Rayleigh number and tectonic reconstruction used as boundary condition.

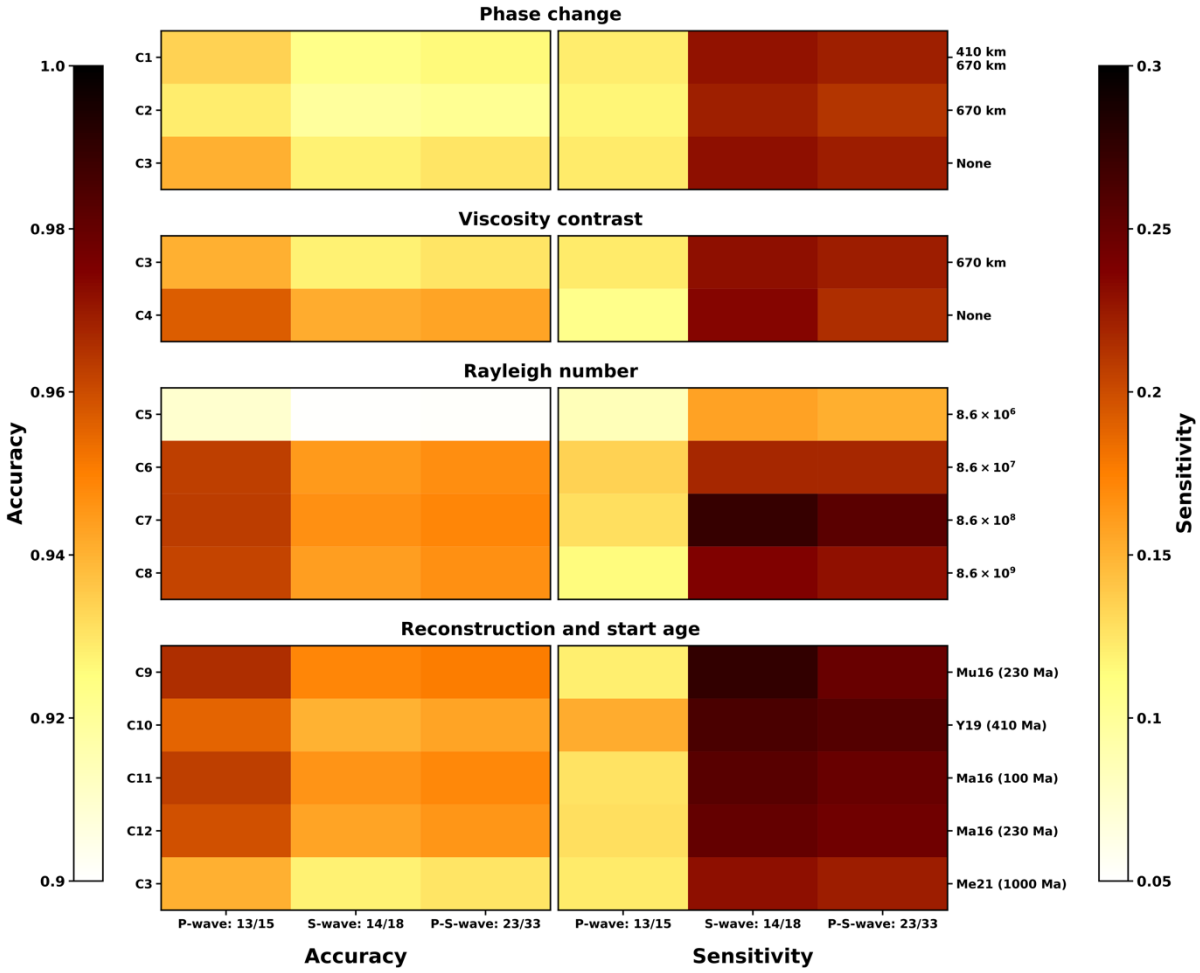

Figure 7. Quantitative match (accuracy on the left-hand-side and sensitivity on the right-hand-side) between mantle 5% colder than ambient and fast seismic anomalies in tomographic models. Different colour maps are used for accuracy and sensitivity. Mantle flow models have been grouped according to their input parameters.

2. Results

2.1. Effect of input parameters on the match to vote maps of tomographic models

We consider the effect of a phase change (cases C1-C3), the viscosity contrast at 660 km depth (cases C3 and C4), the Rayleigh number (cases C5-C8) and the reconstruction (cases C3 and C9-C12).

2.1.1. *Phase Change*

Cases C1-C3 only differ by the considered phase changes: in C1 there are two phase changes at 410 km and 660 km depths, in C2 one phase change at 660 km depth, and in C3 there is no phase change. For these cases, the match to tomographic models is generally good, with minor variations: the accuracy value averaged across tomographic models ($\overline{Acc}$) is 93%, 92% and 92% for C1, C2 and C3 respectively, and the sensitivity value averaged across tomographic models ($\bar{S}$) is 19%, 18% and 19% for C1, C2 and C3 respectively (Fig. 7).

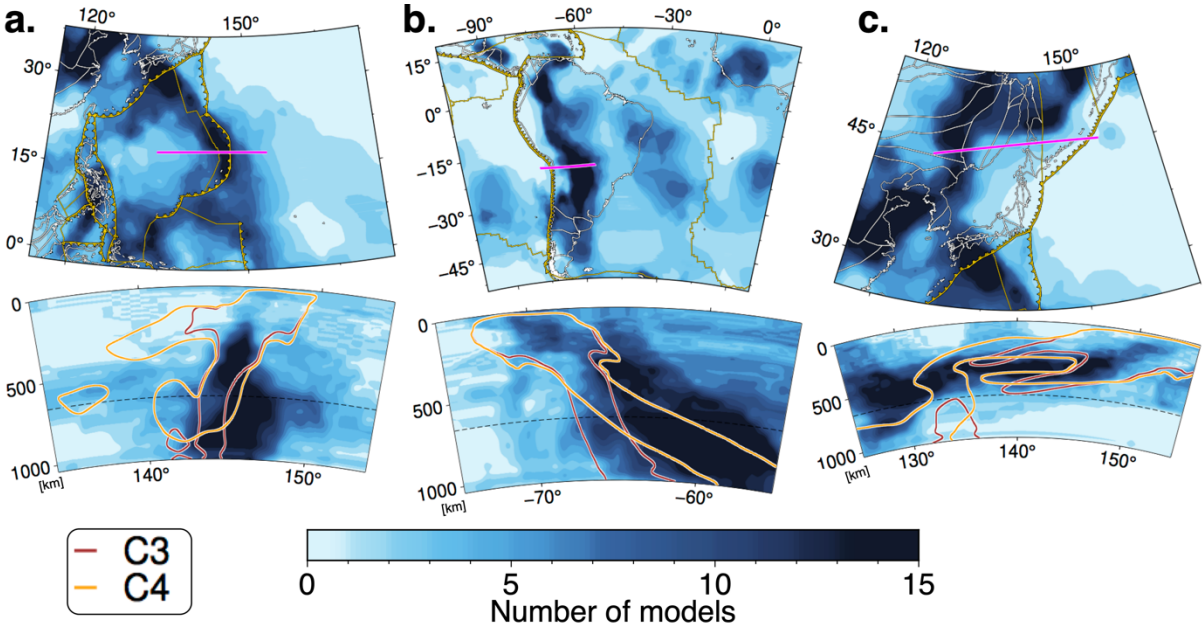

Figure 8. Vote maps for 15 global P-wave tomographic models. (a) Map at 660 km depth and cross-section for the Mariana Trench. (b) Map at 660 km depth and cross-section for South America. (c) Map at 660 km depth and cross-section around Japan. The colour palette is saturated for 13 or more models. On the cross-sections, maroon and orange contours represent models C3 and C4. On the maps, golden lines represent plate boundaries (subduction zone polarities are indicated by symbols), white lines represent coastlines and the transect is shown in magenta. All mantle flow model contours are taken for mantle 5% colder than ambient. The dashed lines on the cross-sections are at 660 km depth.

2.1.2. *Viscosity contrast at 660 km depth*

Cases C3 and C4 only differ by the viscosity contrast at 660 km depth: in case C3 the viscosity pre-factor is ten times greater in the lower mantle than in the upper mantle, whereas it is the same in the upper mantle and lower mantle in case C4. The match to tomographic

388 models was again generally good and similar for these models, with $\overline{Acc}$ equal to 93% and to
389 95% for cases C3 and C4, respectively, and $\bar{S}$ = 19% for both cases. Cross-sections reveal that
390 slabs dip more steeply into the lower mantle for case C4 than for case C3, as expected from the
391 absence of viscosity contrast; this results in an improved visual match for the Mariana slab that
392 is steeply dipping (Fig. 8a), however, in a poorer match for the Farallon and Nazca slab under
393 the Bolivian orocline of South America that penetrates into the lower mantle at a shallower
394 angle (Fig. 8b) and for the Western Pacific slab that stagnates atop the lower mantle (Fig. 8c).
395
396 *2.1.3. Rayleigh number*
397 Cases C5-C8 only differ by the Rayleigh number, which is equal to 8.60×10^6 in case C5,
398 8.60×10^7 in case C6, 8.60×10^8 in case C7, and 8.60×10^9 in case C8. The match to seismic
399 tomographic models is very sensitive to the Rayleigh number. $\overline{Acc}$ and $\bar{S}$ are smallest for case
400 C5, increase as the Rayleigh number is increased to 8.60×10^7 (C6) or 8.60×10^8 (C7), and then
401 decrease again (Fig. 7). $\overline{Acc}$ is equal to 95% for cases C6 and C7, and $\bar{S}$ is equal to 19% and
402 to 21% for cases C6 and C7, respectively (Fig. 7). While the match remains high for
403 $Ra = 8.60 \times 10^9$ (case C8, $\overline{Acc}$ = 95% and $\bar{S}$ = 19%), cross-sections show that the angle of
404 penetration of the slab into the lower mantle increases with the Rayleigh number (Fig. 9).
405 Consequently, C8 slabs best match tomographic model votes on the cross-sections for the
406 steeply dipping Mariana slab, for which C5 slabs are the worst match and C6 and C7 slabs fall
407 in between (Fig. 9a); C8 slabs show the poorest match to the stagnating Western Pacific plate,
408 for which cases C5-C7 predict a stagnating slab (Fig. 9c). Visually, the deep slab dip angles
409 for cases C6 and C7 better matches tomographic models than that for slabs C8 and C5 (Fig.
410 9b). Overall, our preferred Rayleigh number is 8.60×10^8 (C7), which results in good matches
411 to tomographic models globally (Figs 5 and 6) and regionally (Fig. 9), and has been shown to
412 predict slab sinking rates consistent with tomographic constraints (Flament, 2019).

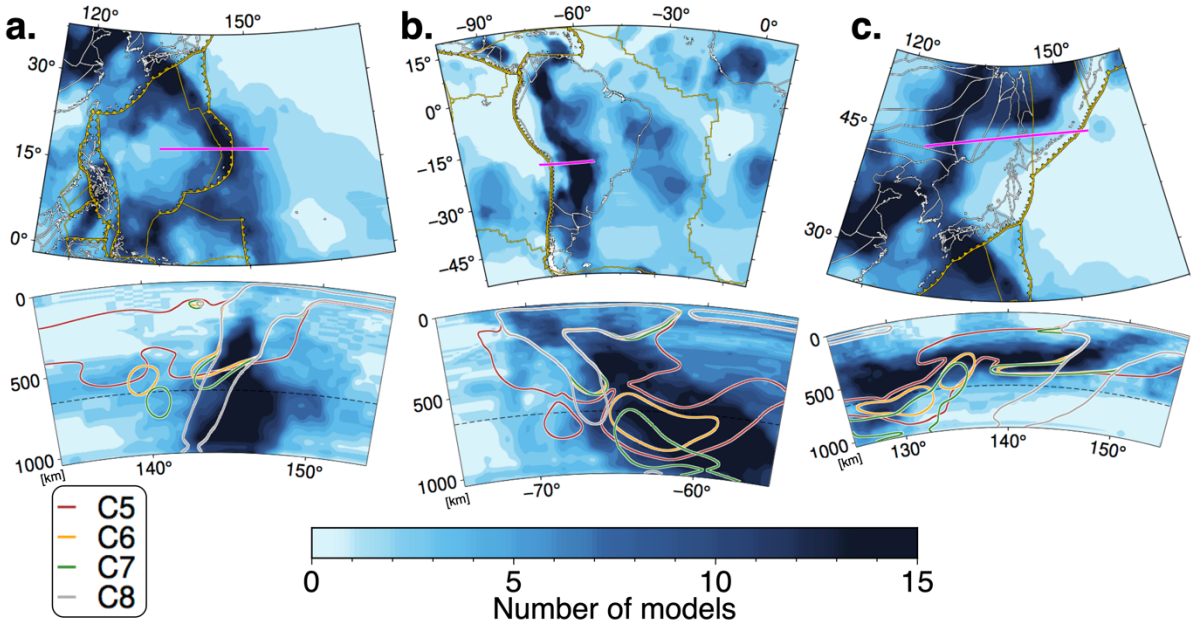

Figure 9. Vote maps for 15 global P-wave tomographic models. (a) Map at 660 km depth and cross-section for the Mariana Trench. (b) Map at 660 km depth and cross-section for South America. (c) Map at 660 km depth and cross-section around Japan. The colour palette is saturated for 13 or more models. On the cross-sections, maroon, orange, green and grey contours represent models C5, C6, C7 and C8 respectively. On the maps, golden lines represent plate boundaries (subduction zone polarities are indicated by symbols), white lines represent coastlines and the transect is shown in magenta. All mantle flow model contours are taken for mantle 5% colder than ambient. The dashed lines on the cross-sections are at 660 km depth.

2.1.4. Tectonic reconstruction

We varied the tectonic reconstruction used as surface boundary condition across mantle flow model cases C3 and C9-C12 (Table 1). The model start age a_0 was also varied across these model cases between 100 Ma and 1000 Ma (Table 1); while a_0 should be greater than ~250 Ma to investigate predicted deep mantle structure (Flament, 2019), a_0 = 100 Ma is sufficient for slabs to sink down to 1000 km depth with the selected Rayleigh number and viscosity structure (Flament, 2019). For these cases, 93% < $\overline{Acc}$ < 95% with a maximum for C9 (Fig. 7), and 19% < $\overline{S}$ < 22% with a minimum for C3 and a maximum for C10 (Fig. 7). At the three considered locations, this series of cases generally matches tomographic models, although with

some variability in the prediction of slab material between model cases (Fig. 10). Cases C3 (based on reconstruction Me21) and C10 (based on reconstruction Y19) generally predict similar deep slab dip angles, which is expected since reconstruction Me21 extends reconstruction Y19 further back in time, although Case C3 tends to predict a greater amount of slab material in the upper mantle compared to other cases. Both cases match tomographic models at locations with penetrating and stagnating slabs (Fig. 10). Cases C9 (Mu16) and C12 (Ma16) also share similarities with each other, notably predicting slab break offs at approximately 660 km depth (Fig. 10); C9 predicts slabs that penetrate more steeply into the lower mantle due to the absence of a viscosity contrast. Out of these cases, C11 (Ma16) predicted the thinnest slabs and the most rapid changes in dip angle between 650 km depth and 900 km depth, including a prominent slab break off and offset at the Mariana Trench, which is not consistent with tomographic models (Fig. 10a). Overall, case C10 is preferred, because it predicts slabs that best match tomographic vote maps globally, and with geometries compatible with tomographic models at the three selected locations.

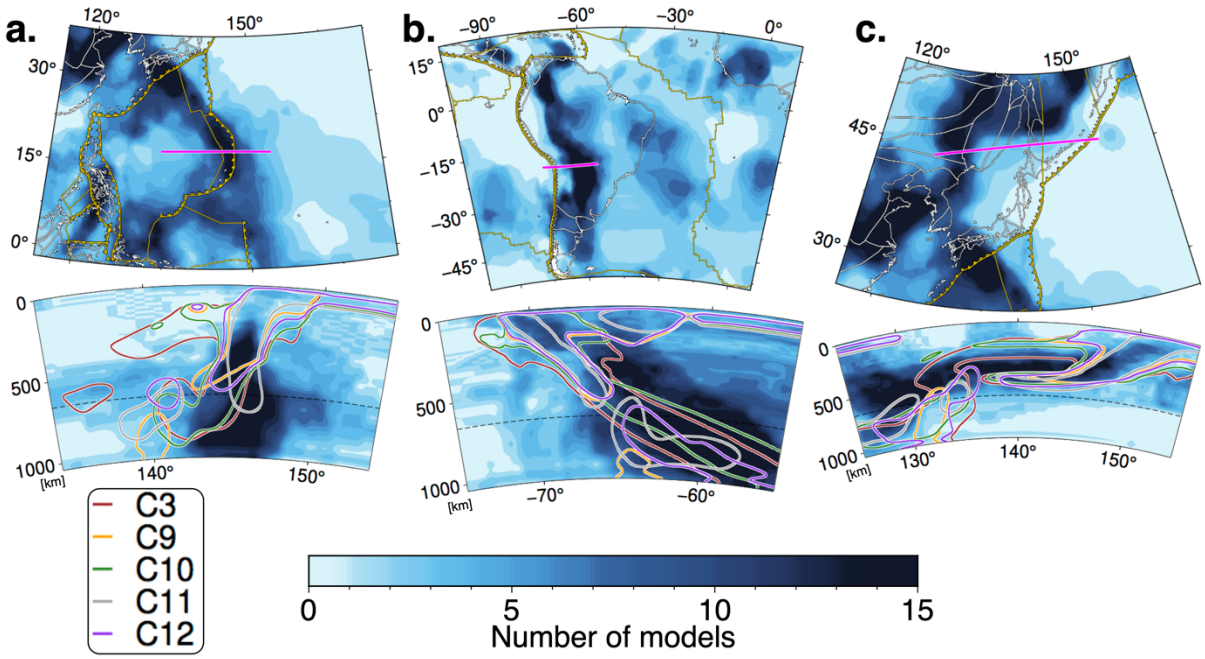

Figure 10. Vote maps for 15 global P-wave tomographic models. (a) Map at 660 km depth and cross-section for the Mariana Trench. (b) Map at 660 km depth and cross-section for South America. (c) Map at 660 km depth and cross-section around Japan. The colour palette is

saturated for 13 or more models. On the cross-sections, maroon, orange, green, grey and purple contours represent models C3, C9, C10, C11 and C12 respectively. On the maps, golden lines represent plate boundaries (subduction zone polarities are indicated by symbols), white lines represent coastlines and the transect is shown in magenta. All mantle flow model contours are taken for mantle 5% colder than ambient. The dashed lines on the cross-sections are at 660 km depth.

2.2.Evolution of predicted deep slab dip angles through time

We analyse the evolution of predicted deep slab dip angles for preferred case C10 for models with contrasted Rayleigh number and input tectonic reconstruction because these were found to be the two factors that most affected present-day deep slab dip angle in the previous section.

2.2.1. Effect of the Rayleigh number

The match between mantle flow models and tomographic models is very sensitive to the Rayleigh number (Fig. 7). Here, we investigate the evolution of predicted deep slab dip angles for continuous subduction at the Mariana Trench from 48 Ma (Fig. 11) and under Japan from 79 Ma (Fig. 12) for model cases based on contrasted Rayleigh numbers. Maps of mantle temperature at 660 km depth give a sense of the deep slab dip angles in the upper mantle: because subduction zones exist for the entire period represented on the figure, larger distances between the trench (in green with symbols for polarity, at the surface) and cold temperature anomalies at 660 km indicate that the trench has rolled back since the slab was anchored into the lower mantle (Figs 11 and 12). Cross-sections in the mantle frame of reference (i.e., not moving with plates) show that the Mariana Trench rolled back between 48 Ma and 28 Ma and has been largely stable from 28 Ma (Fig. 11). In contrast, subduction of the Izanagi and Western Pacific plate to the north of the Japanese Islands was stable between 79 Ma and 58 Ma and

476 rolled back in the last 18 Myr (Fig. 12). Our results indicate that trench motion affects deep
477 slab dip angle.

478 At the Mariana Trench, C8 slabs (largest *Ra*) penetrate the lower mantle at a high angle by
479 28 Ma, and this behaviour persists until the present day with a minor slab break off event at
480 8 Ma (Fig. 11). In contrast, C5 slabs (lowest *Ra*) have accumulated in the upper mantle and
481 stagnated atop the lower mantle from 28 Ma (Fig. 10), which is not consistent with tomographic
482 models (Fig. 9). Cases C6 and C7 predict a slab break-off from 8 Ma, with penetration into the
483 lower mantle in the last 8 Myr, offset westward from the trench (Fig. 11), which is not
484 consistent with tomographic models either (Fig. 9).

485 To the north of the Japanese Islands, the Izanagi slab dipped at ~60º in the upper mantle
486 between 79 Ma and 58 Ma, and the dip angle into the lower mantle was variable: it was steep
487 for case C8 (largest *Ra*) at 79 Ma and 58 Ma, and steepened from a shallow dip between 79 Ma
488 and 58 Ma for all other cases (Fig. 12). As the trench rolled back, the dip angle decreased in
489 the upper mantle for cases C5-C7, however, the dip angle into the lower mantle remained large
490 for case C8 (largest *Ra*) so that the slab penetrates the lower mantle without stagnating into the
491 upper mantle at present day, which is not consistent with tomographic models (Fig. 9). Case
492 C5 (smallest *Ra*) predicts the largest offset between the trench and penetration into the lower
493 mantle, although this offset is still smaller than in tomographic models (Fig. 9). Cross-sections
494 of tomographic votes suggest that the volume of stagnating slabs is between that predicted by
495 case C5 and by cases C6 and C8 (Fig. 9), although this visual comparison depends on selected
496 thresholds (Fig. 6). Overall, these results suggest that the Rayleigh number alone cannot be
497 adjusted to fit contrasted deep slab dip angles, and that regional variations in the viscosity
498 structure of the mantle could account for imaged deep slab dip angles.

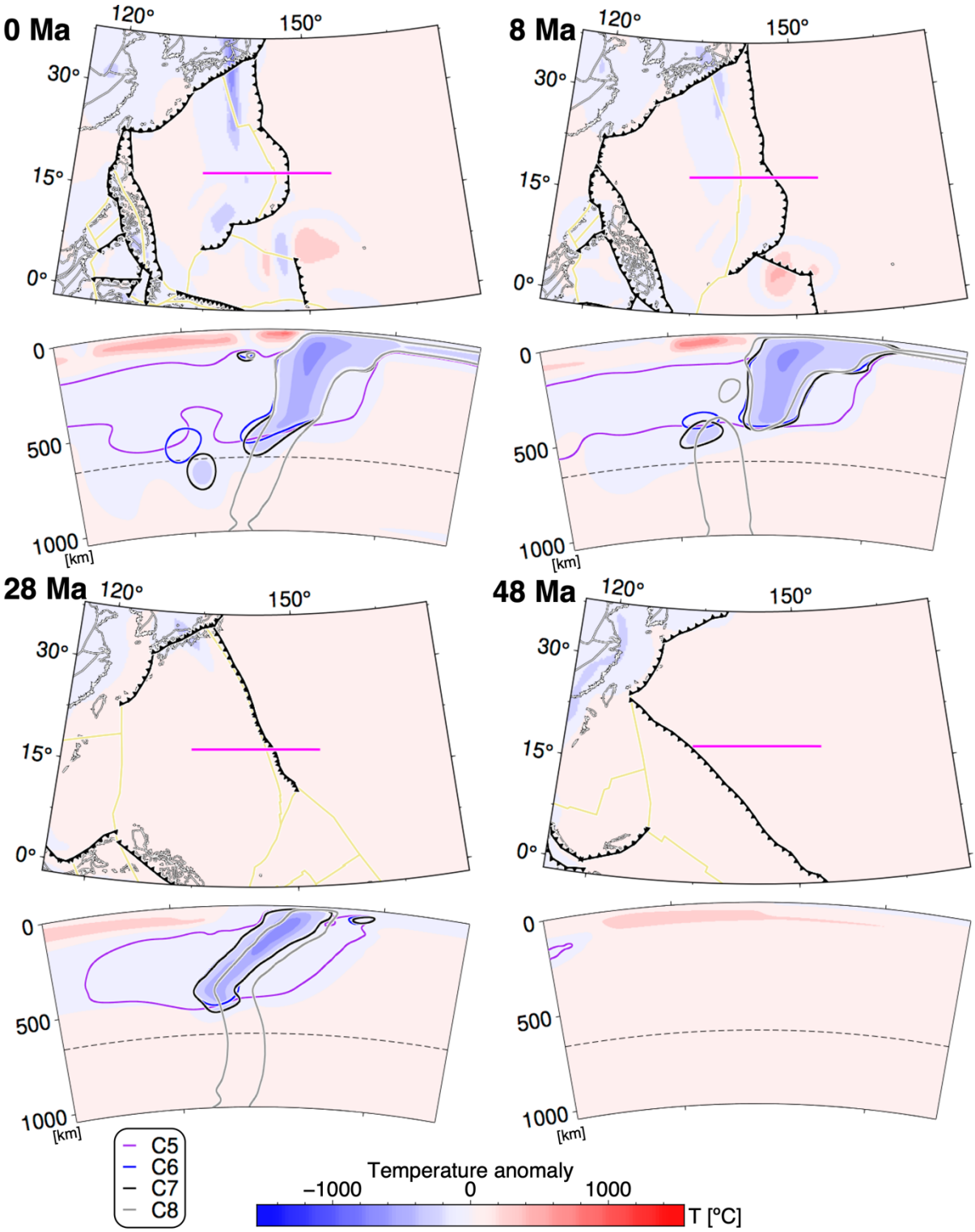

Figure 11. Cross-sections of mantle flow models based on different Rayleigh numbers through time, taken under the Mariana Trench. Purple, blue, black and grey contours on cross-sections represent models C5, C6, C7 and C8 (note that C8 is shown at 0 Ma, 9 Ma, 29 Ma and 48 Ma, resulting in a slight offset). The predicted mantle temperature anomaly is shown at 660 km depth for C7. On the maps, black lines represent subduction zones, grey lines represent coastlines, khaki lines represent mid-ocean ridges and transform faults, and magenta line the location of the cross-section. The dashed lines on the cross-sections are at 660 km depth.

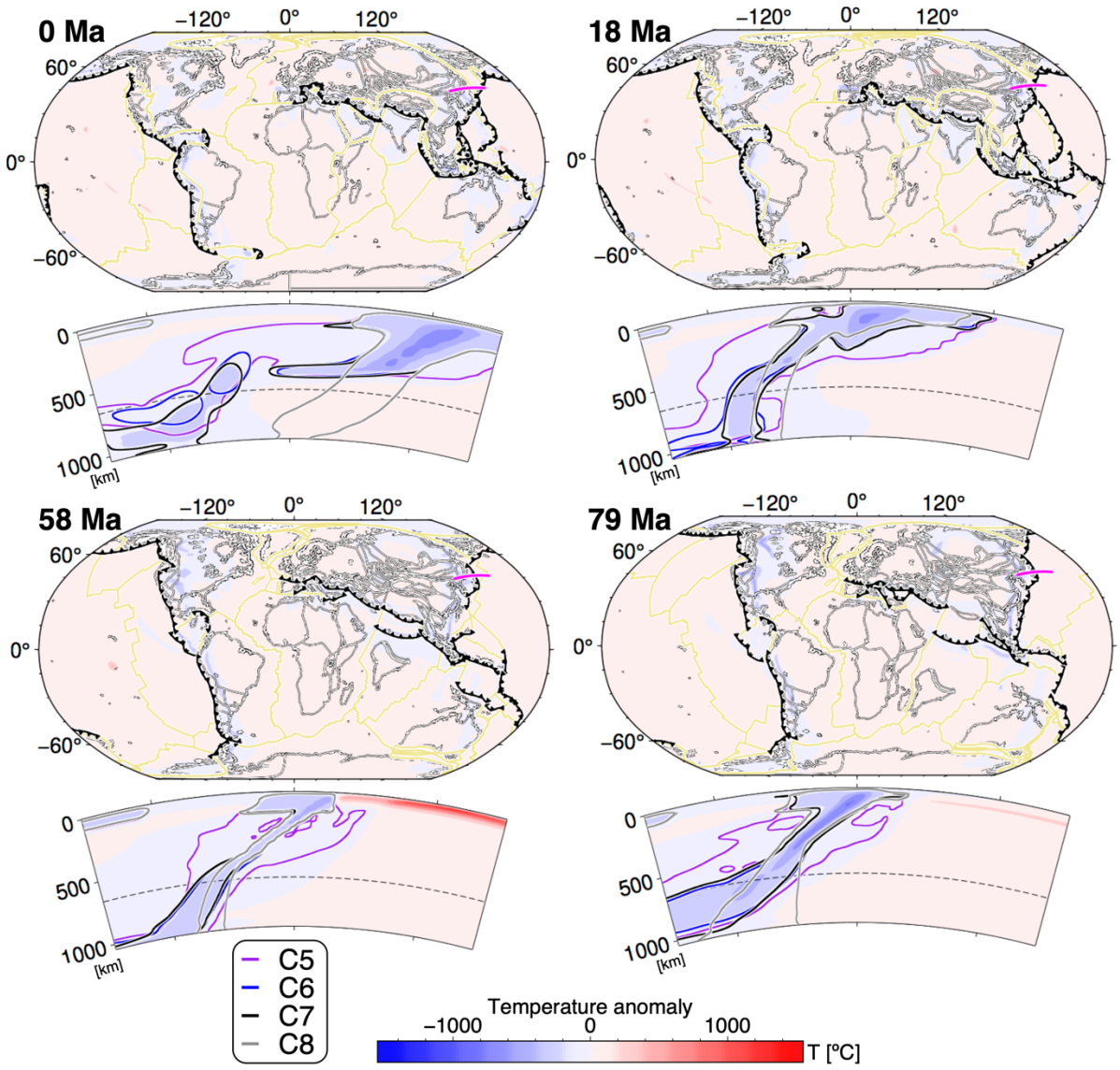

Figure 12. Cross-sections showing the evolution of temperature predicted by mantle flow models based on different Rayleigh numbers, taken under Japan. Purple, blue, black and grey contours on cross-sections represent models C5, C6, C7 and C8 (note that C8 is shown at 0 Ma, 19 Ma, 59 Ma and 78 Ma, resulting in a slight offset). The predicted mantle temperature anomaly is shown at 660 km depth for C7. On the maps, black lines represent subduction zones, grey lines represent coastlines, khaki lines represent mid-ocean ridges and transform faults, and magenta line the location of the cross-section. The dashed lines on the cross-sections are at 660 km depth.

2.2.2. Effect of the tectonic reconstruction

The subduction history is overall very similar in cases C9 (reconstruction Mu16), C10 (reconstruction Y19) and C12 (reconstruction Ma16); trenches in reconstructions Mu16 and

519 Ma16 are near identical, with differences at ~19 Ma in Southeast Asia and along the Arabian
520 Peninsula (Fig. 14), and more significant differences at 79 Ma for the configuration of
521 subduction between India and Asia and along Oman (Fig. 14). There are more differences
522 between reconstructions Y19 and Mu16, which reflect 1/ the use of different reference frames:
523 Torsvik et al. (2008) in Mu16, and Torsvik and Voo (2002) in Y19, 2/ the use of deforming
524 plate boundary zones (Müller et al., 2019) in the versions of tectonic reconstructions Mu16 and
525 Ma16 presented here, but not in reconstruction Y19 – this effect is most prominent for South
526 America at 79 Ma (Fig. 13) – , 3/ as well as differences in relative plate motions: reconstruction
527 Y19 includes a slab to the east of the Arabian Peninsula at 79 Ma to account for the
528 emplacement of the Oman ophiolite (Searle and Cox, 2002), two subduction zones between
529 India and Eurasia (Jagoutz et al., 2015), and differences in the subduction history to the North
530 of Australia and around the Philippine Sea plate (Zahirovic et al., 2016).

531 At the Mariana Trench, results for all three model cases are similar at 39 Ma and at
532 29 Ma (Fig. 13). At 9 Ma, the slab is further to the east in C10 (Y19) than in C9 (Mu16) and
533 C12 (Ma16), and because this location is more similar to the present-day location of the trench,
534 this results in a C10 slab that is continuous and steeply dipping into the lower mantle at present-
535 day (Fig. 13), which is consistent with tomographic models (Fig. 10), whereas C9 and C12
536 slabs are not continuous and offset with respect to tomographic models (Figs 10 and 13). The
537 C9 slab dips more steeply into the lower mantle than the C12 slab, which is expected in the
538 absence of a viscosity contrast at 660 km depth in C9 (Table 1). The slab volume is greater in
539 C10 than in C9 and C12 because the thickness of the oceanic lithosphere and shallow slabs
540 was built with a half-space cooling assuming a maximum lithospheric age of 80 Ma in C9 and
541 C12, and without a maximum in C10.

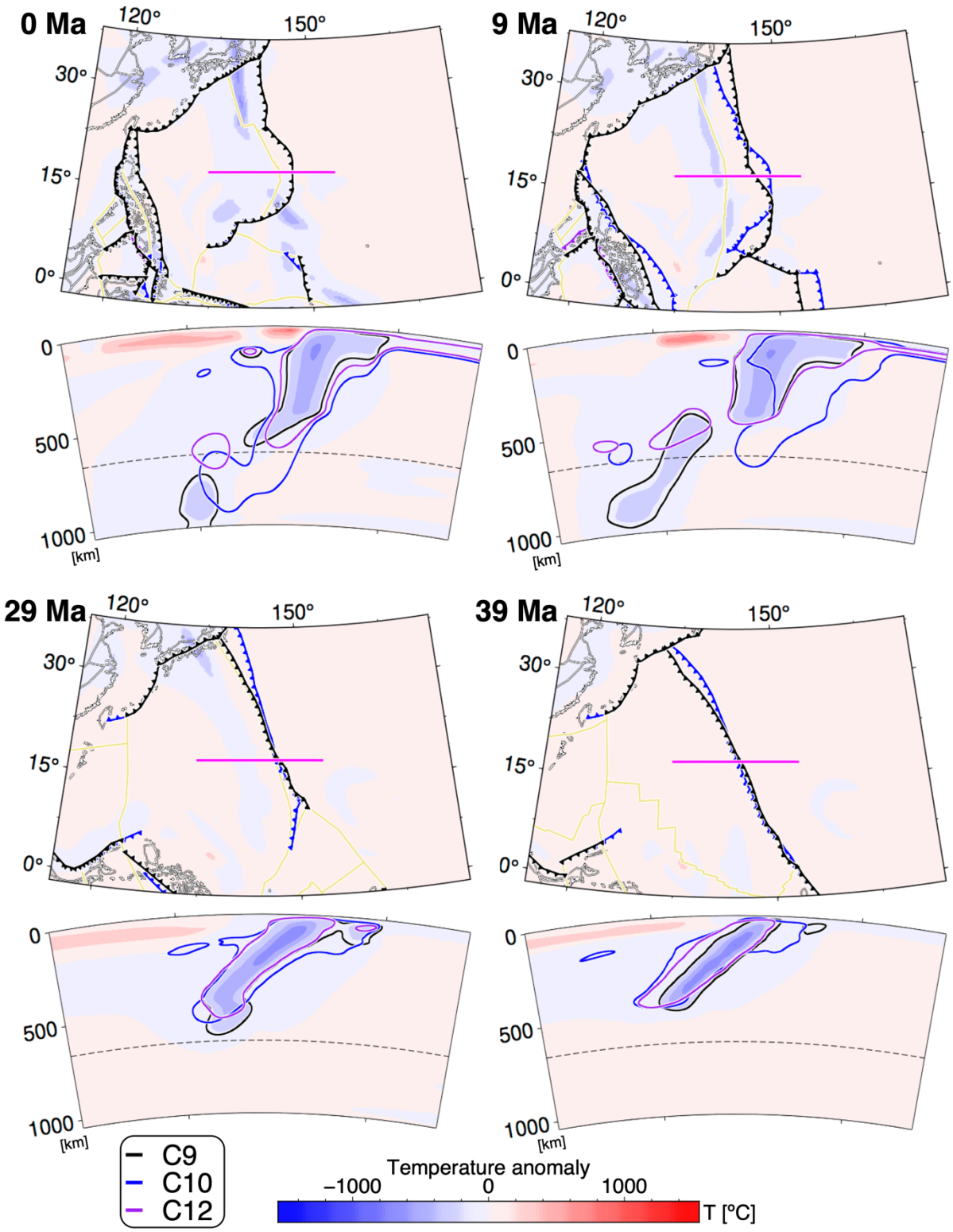

Figure 13. Cross-sections showing the evolution of temperature predicted by mantle flow models based on different tectonic reconstructions, taken under the Mariana Trench. Black, blue and purple contours on the cross-sections represent models C9, C10 and C12 respectively. The predicted mantle temperature anomaly is shown at 660 km depth for C9. On the maps, black, blue and purple lines represent subduction zones for models C9, C10 and C12

548 respectively. Grey lines represent coastlines, khaki lines represent mid-ocean ridges and
549 transform faults for case C9, and magenta line the location of the cross-section. The dashed
550 lines on the cross-sections are at 660 km depth.
551
552 Differences between cases C9, C10 and C12 are smaller the north of the Japanese
553 Islands. At 79 Ma, the trench is slightly offset to the east in C10 compared to C9 and C12, slab
554 dip angles are similar across cases in the upper mantle, and steeper for C9 in the lower mantle
555 in the absence of a viscosity contrast. All three cases are similar at 29 Ma, with a ~60º dip in
556 the upper mantle that steepens to ~80º in the lower mantle for cases C10 and C12 whereas slab
557 C9 is broken off at ~950 km depth. The lateral offset between the trench and the anchor point
558 in the lower mantle increases from 29 Ma to the present in all three models, and while the
559 stagnation in the upper mantle is consistent with tomographic models, the lateral offset between
560 the trench and the entry point into the lower mantle is smaller in all three cases than in
561 tomographic models, and the slab is continuous in tomographic models whereas it is not in the
562 flow models (Figs 10 and 14). These two features suggest that changes to tectonic
563 reconstructions of this area may be required: the slab breakoff in the models (Figs 10 and 14)
564 suggests that the subduction rate is too small with respect to the trench rollback, and the larger
565 lateral offset in tomographic models than in flow models (Fig. 10) suggests that the trench
566 should initially be ~100 km further west back in time (at ~80 Ma), which would lead to the
567 slab anchoring into the lower mantle further west (Fig. 14) and to trench rollback over a greater
568 distance but also over a longer period.
569
570 *2.2.3. Tectonic origins of penetrating and stagnating slabs*
571 The shape of the reconstructed Mariana Trench changed from a near straight subduction
572 zone between 49 Ma and 29 Ma, to a curved trench system in the last 19 Myr. The trench rolled
573 back between 49 Ma and 29 Ma and it has been largely stable since then, which for case C10

leads to the development of a continuous slab that dips steeply into the upper mantle then shallowing into the top of the upper mantle (Figs 13 and 15). This prediction is generally consistent with tomographic models, although the imaged slab penetrates the lower mantle at a steep angle, and down to 1000 km as opposed to ~950 km depth (Fig. 10).

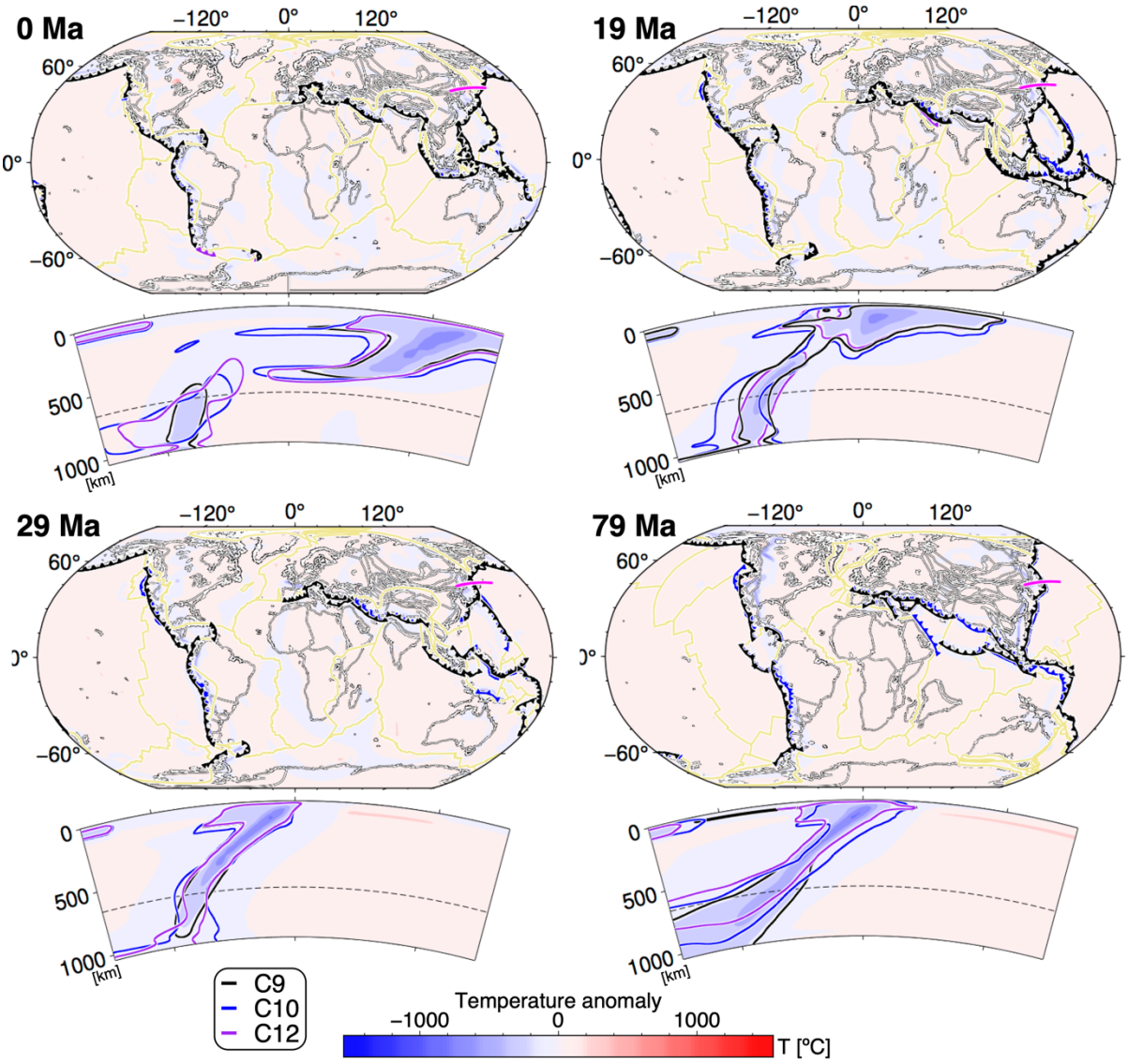

Figure 14. Cross-sections showing the evolution of temperature predicted by mantle flow models based on different tectonic reconstructions, taken under Japan. Black, blue and purple contours on the cross-sections represent models C9, C10 and C12 respectively. The predicted mantle temperature anomaly is shown at 660 km depth for C9. On the maps, black, blue and purple lines represent subduction zones for models C9, C10 and C12 respectively. Grey lines represent coastlines, khaki lines represent mid-ocean ridges and transform faults for case C9, and magenta line the location of the cross-section. The dashed lines on the cross-sections are at 660 km depth.

In reconstruction Y19 that does not account for deformation, the South American trench along the Bolivian orocline retreated by ~19º westward since 79 Ma from ~52ºW to ~71ºW (Fig. 16); the total amplitude of this retreat would be smaller in models accounting for Andean mountain building (Fig. 14; Müller et al., 2019). The point of slab penetration into the lower mantle migrated by ~16º over the same period, from ~48ºW to ~64ºW, leading to a shallowing of the slab over time, which is more pronounced in the lower mantle than in the upper mantle: At 49 Ma, the predicted slab dipped at ~60º down to 1000 km depth; by 29 Ma, the slab bent into the lower mantle, and at 0 Ma, the slab dips at ~50º in the upper mantle and ~30º in the lower mantle (Fig. 16). Tomographic models suggest that the slab dips steeply into the lower mantle, which is more consistent with tectonic reconstructions that account for the deformation of the South American continent (e.g., case C12 in Fig. 10b).

To the north of the Japanese Island, the trench is reconstructed to have been largely stable between 79 Ma and 29 Ma, and to have retreated in the last 19 Myr. The slab predicted for case C10 penetrated into the lower mantle at 79 Ma with a dip of ~60º down to 660 km depth and stagnation further west (dip ~0º) at ~900 km depth; at 29 Ma the dip was ~60º in the upper mantle and nearly vertical into the lower mantle; at 19 Ma the dip was ~50º in the upper mantle and vertical into the lower mantle, and at present-day the slab stagnates in the lower mantle and in the uppermost lower mantle. These results illustrate the effect of trench retreat on deep slab dip angle. As mentioned above, revisiting the initial location of the Izanagi and Western Pacific trench and the timing of trench retreat could improve the match between mantle flow models and tomographic models at this location (Fig. 10).

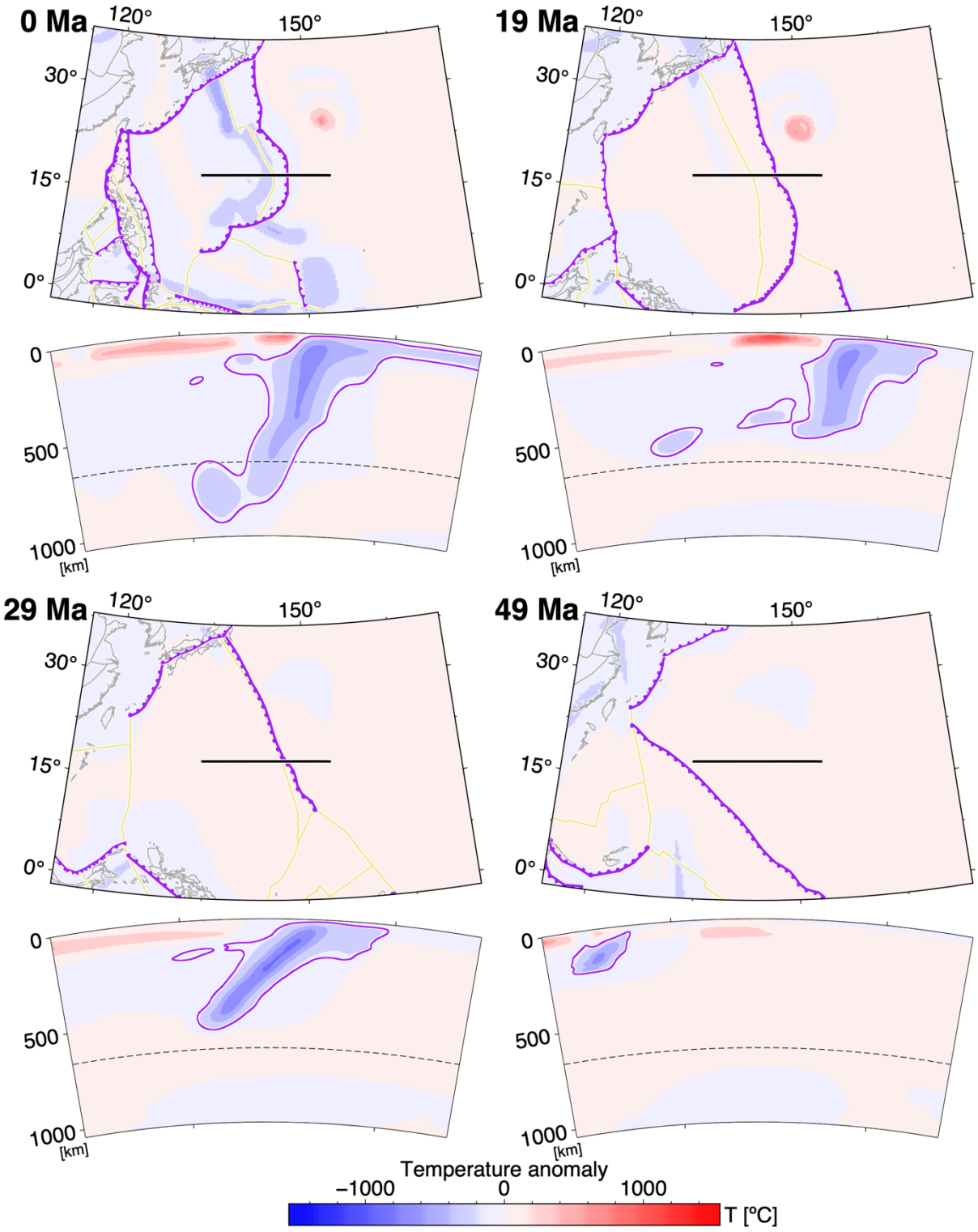

608 **Figure 15.** Cross-sections of model C10 through time, taken under the Mariana Trench. The
609 top panels show the regional reconstruction for the Mariana Trench through time. The predicted
610 mantle temperature anomaly is shown at 660 km depth for C10. Purple lines represent
611 subduction zones, grey lines represent coastlines, and khaki lines represent mid-ocean ridges
612 and transform faults.
613

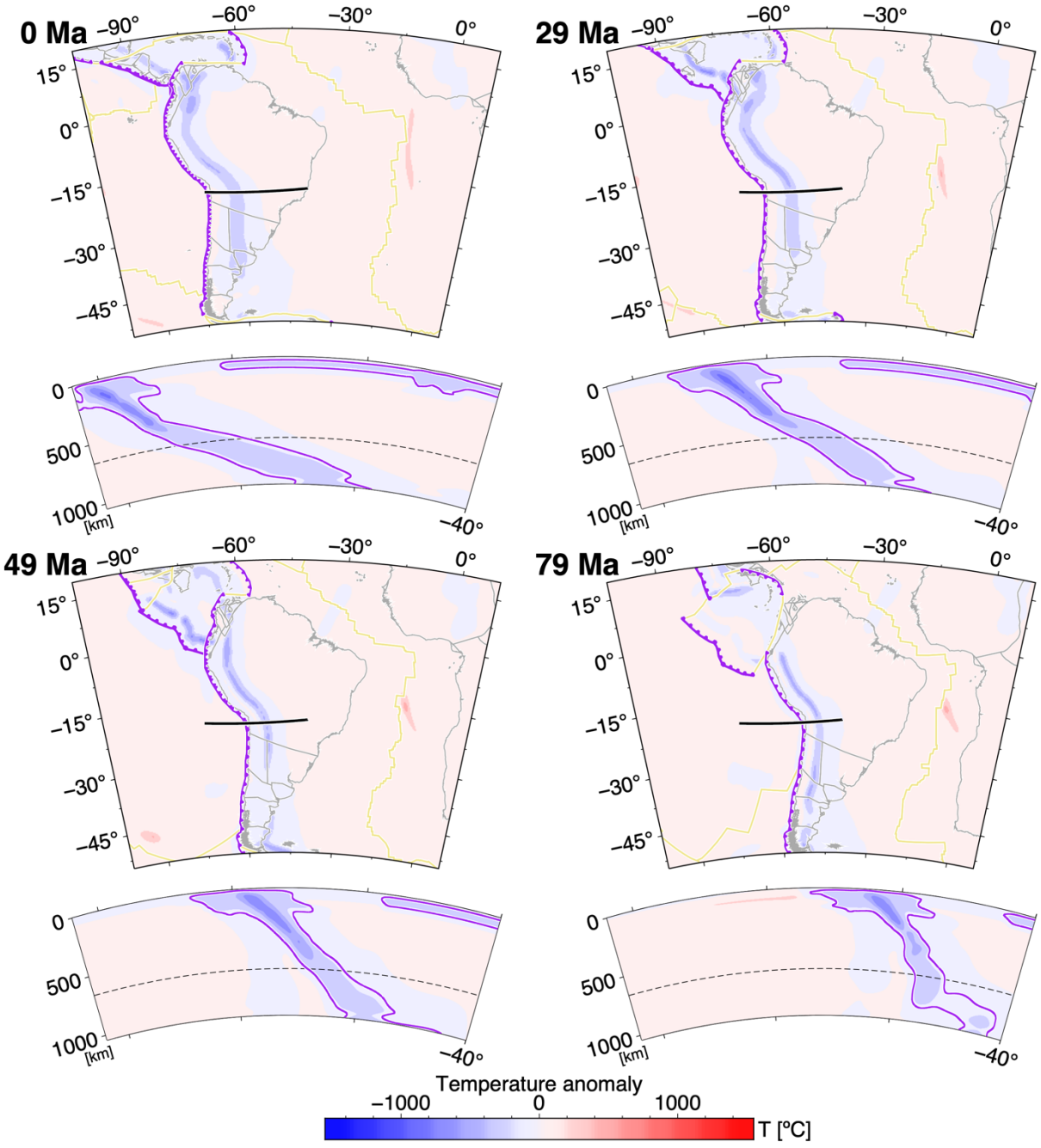

614 **Figure 16.** Cross-sections of C10 through time, taken under South America. The top panel
615 shows the regional reconstruction for South America through time. The predicted mantle
616 temperature anomaly is shown at 660 km depth for C10. Purple lines represent subduction
617 zones, grey lines represent coastlines, and khaki lines represent mid-ocean ridges and transform
618 faults.
619

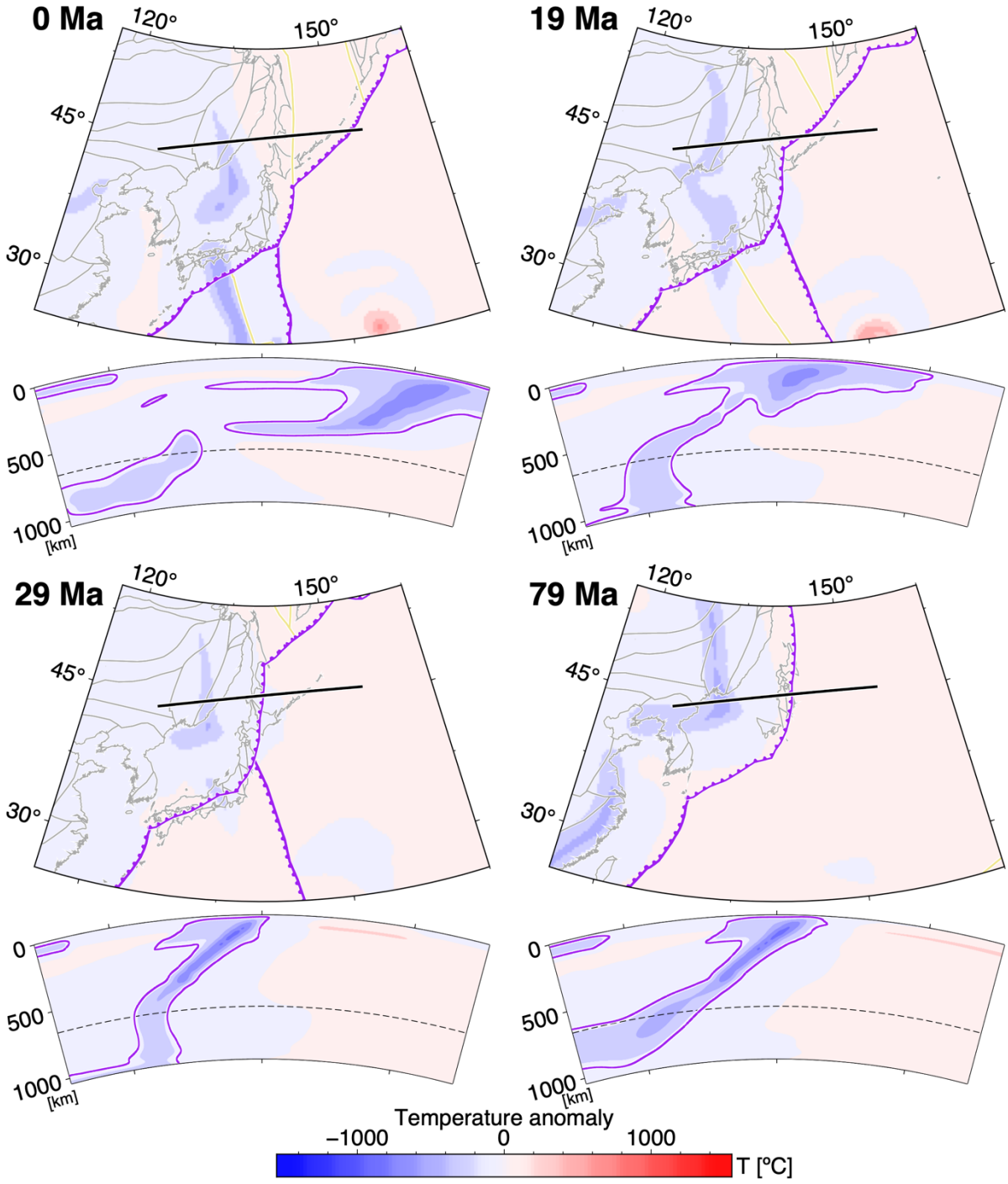

Figure 17. Cross-sections of model C10 through time, taken under Japan. The top panel shows the regional reconstruction for East Asia through time. The predicted mantle temperature anomaly is shown at 660 km depth for C10. Purple lines represent subduction zones, grey lines represent coastlines, and khaki lines represent mid-ocean ridges and transform faults.

3. Discussion

4.1. Factors contributing to deep slab dip angle

The main factors affecting deep slab dip angle that were investigated in this study were phase changes, the viscosity contrast at 660 km depth, the Rayleigh number and the tectonic reconstruction.

3.1.1. Phase change.

We found that considering phase changes at 410 km and 660 km depth only has a minor effect on model results. Agrusta et al. (2017) used fully dynamic models to show that phase transitions affect the evolution of deep slab dip angle through time. This difference could reflect that imposing surface plate velocities and the thermal structure of slabs down to 350 km controls mantle dynamics down in our models. Because large-scale mantle flow influences the location and deep dip angle of slabs (Peng and Liu, 2023), we suggest that the effect of phase changes on the interaction of slabs with the transition zone could be investigated in fully-dynamic global convection models (e.g., Coltice et al., 2019).

3.1.2. Viscosity contrast at 660 km depth.

We found that the presence of a viscosity increase at 660 km depth was required to explain stagnating slabs, consistently with previous work (e.g., Čížková and Bina, 2019). An increase by a factor of ten was sufficient for slabs to stagnate, although viscosity also increases with pressure (and therefore depth) in our models. In the absence of a viscosity increase with depth, all slabs dip steeply into the lower mantle which does not match tomographic constraints (Fig. 8). We did not investigate the effect of a thin low-viscosity layer beneath the transition zone which has been proposed to favour slab stagnation and improve the qualitative match between

653 slabs predicted by tectonically-driven mantle flow models and imaged by tomographic models
654 (Mao and Zhong, 2018). We find that slab stagnation occurs in our models in the absence of a
655 low-viscosity layer beneath the transition zone (Figs 8-10, 12, 14) and note that the models of
656 Mao and Zhong (2018) used the Boussinesq approximation, which is known to result in
657 excessive slab volume (Flament, 2019). The effect of a thin low-viscosity layer beneath the
658 transition zone on slab stagnation could be investigated in future models using the extended-
659 Boussinesq or truncated anelastic liquid approximation.
660
661 *3.1.3. Rayleigh number.*
662 The Rayleigh number affects the vigour of convection, and in turn the dip angle of slabs:
663 models with a large $Ra = 8.60 \times 10^9$ resulted in slabs penetrating the lower mantle nearly
664 vertically, while models with a low $Ra = 8.60 \times 10^6$ resulted in slabs stagnating in the upper
665 mantle (Figs 9, 11 and 12). Intermediate deep slab dip angles were obtained for $8.60 \times 10^7 <$
666 $Ra < 8.60 \times 10^8$. The Rayleigh number influences the slab sinking rate and the CMB heat flow
667 (because Ra is proportional to the temperature drop across the mantle ΔT). Flament (2019)
668 compared these two metrics to independent constraints and preferred model cases with $Ra =$
669 8.60×10^8.
670
671 *3.1.4. Tectonic reconstruction and trench motion.*
672 Previous work has shown that fast trench motions (2-4 cm/yr) can cause a slab to flatten at
673 the upper-lower mantle boundary (van der Hilst and Seno, 1993; Griffiths et al., 1995;
674 Christensen, 1996; Olbertz et al., 1997) and that in contrast, limited trench retreat can result in
675 the penetration of a slab through this 660 km discontinuity, sinking through to the lower mantle
676 (van der Hilst and Seno, 1993). Our models confirm these findings: we find that the stability
677 of the Mariana Trench leads to steeply dipping slab, whereas the fast retreat of the trench to

678 the east of Japan over the last 19 Myr leads to the stagnation of the Pacific slab atop the upper
679 mantle following a period during which the slab penetrated into the lower mantle when the
680 trench was stable (79 Ma – 29 Ma). The scenario along South America also illustrates how
681 changes in trench motion are reflected in deep slab dip angles, with trench retreat leading to a
682 shallowing of the dip angle in the upper mantle (in the flow models). Trench retreat may lead
683 to slab break off (Fig. 17), and we find that the retreat of the Izanagi and Western Pacific trench
684 should start further west than in the reconstruction to match the anchoring of the slab and occur
685 at a lower rate (over a longer period) to avoid slab breakoff since this is not imaged by
686 tomographic models (Fig. 10c). Indeed, recent studies have used mantle tomography (Wu et
687 al., 2022) or mantle flow models (Ma et al., 2019) to improve tectonic reconstructions for East
688 Asia for the last ~120 Myr.
689 Further potential contributing factors to deep slab dip angles include slab age and
690 subduction velocity (e.g., Goes et al., 2017). While these factors are more tractable in two-
691 dimensional subduction models than in our global reconstructions of past mantle flow, they
692 could be investigated in future investigations of our models.
693
694 *4.2. Strengths and limits of our approach*
695
696 *4.2.1. Mantle flow models*
697 The mantle flow models used in this study can be directly compared to independent
698 spatial constraints on mantle convection because they use tectonic reconstructions as boundary
699 conditions to simulate past mantle convection. Here, we compare the present-day temperature
700 predicted by our forward mantle flow models to tomographic models from which they are
701 mostly independent. The initial temperature structure of our forward mantle flow models is not
702 derived from tomographic models. In this respect, our reconstructions of mantle flow are

703 independent from tomographic models, compared to approaches that use tomographic models
704 to model mantle flow (e.g., Steinberger and Calderwood, 2006). In our models, in order to
705 obtain one-sided subduction with lateral resolution ~50 km and lateral viscosity variations over
706 three orders of magnitude, the shallow portion of subducting slabs is calculated analytically
707 and blended in with the solution for mantle convection down to ~ 350 km depth, making it
708 possible to quantitatively compare mantle flow and tomographic models between 396 km and
709 1,040 km depths.

710 A separate approach imposing plate velocities, the thermal structure of the lithosphere,
711 as well as viscosity and buoyancy variations in the vicinity of subduction zones makes it
712 possible to predict the shallow slab dip angle in mantle flow models extending back ~150 Ma
713 (Hu et al., 2018). Yet another approach consists of investigating the deep slab dip angles
714 obtained by varying parameters in fully dynamic models, usually in two dimensions, and
715 qualitatively comparing results to independent tomographic models. This approach is powerful
716 to identify the effect of the viscosity structure (Čížková and Bina, 2019), rheology (Garel et
717 al., 2014), and phase changes (Agrusta et al., 2017) on deep slab dip angle, however, it is not
718 as direct to compare results to constraints. However, two-dimensional or three-dimensional
719 regional models do not capture the effect large-scale mantle flow on the location and dip angle
720 of slabs (Peng and Liu, 2023). Predicting the evolution of deep slab dip angles in fully dynamic
721 global models requires resolutions of the order of one kilometre and large lateral viscosity
722 contrasts (six order of magnitude or more; Stadler et al., 2010; Coltice et al., 2019), both of
723 which remain computationally challenging in global mantle flow models and have only been
724 achieved using adaptive mesh refinement in models of present-day mantle flow (Stadler et al.,
725 2010). Lower resolution models with large lateral viscosity contrasts predict one-sided
726 subduction zones alongside continents, but two-sided intra-oceanic subduction zones (Coltice
727 et al., 2019).

728 *4.2.2. Tomographic models and vote maps*

729 The interaction between slabs and the transition zone leads to interesting geodynamic
730 questions related to contrasted deep slab dip angles (e.g., Garel et al., 2014; Goes et al., 2017;
731 Čížková and Bina, 2019) which motivated this study. While vote maps of global tomographic
732 models reveal fast-velocity anomalies that we interpreted as slabs (e.g., Fig. 4), this mapping
733 is limited because global tomographic models poorly constrain the structure of the mantle
734 between ~400 km and 1000 km depth, although this can be improved by including surface
735 wave overtones (Ritsema et al., 2004). We primarily focused on P-wave tomographic models
736 because these better resolve slabs beneath dense seismic networks (Supplementary Figure 1),
737 although S-wave tomographic models achieve a better global coverage (Supplementary
738 Figure 2) (Grand, 2002; Ritsema et al., 2004). We assumed that positive seismic velocity
739 anomalies represent cold mantle and therefore slabs, and we did not consider the influence of
740 chemical variations that may be significant in the lower 1000 km of the mantle (Trampert et
741 al., 2004).

742 The selection of tomographic models from which to derive vote maps influences the result.
743 Here we selected a large number of global tomographic models following early work with vote
744 maps (Shephard et al., 2017; Coltice and Shephard, 2018) and to capture information from as
745 many tomographic models as possible. We note that our selection of tomographic models
746 includes three DETOX models from Hosseini et al. (2020), which results in an over-
747 representation of the features common to these three similar global tomographic models. An
748 alternative approach would consist of selecting a subset of tomographic models representative
749 of the data types and processing techniques used in tomographic inversions (Shephard et al.,
750 2021). Investigating the match between individual tomographic models and mantle flow
751 models is also tractable when fewer tomographic models are considered (e.g., Peng and Liu,

752 2023) or when the data are reduced using spherical harmonics correlations (Becker and Boschi,
753 2002) or cluster analysis (Flament et al., 2022).
754
755 *4.2.3. Inferring the location of past subduction zones from tomographic models*
756 While mantle flow models predict subducted slabs, a complementary approach consists
757 of mapping slabs in tomographic models, and matching them with geological evidence of past
758 subduction at Earth's surface to infer the past location of subduction zones (Wu et al., 2016;
759 Zahirovic et al., 2016; Van der Meer et al., 2018); this approach requires selecting a threshold
760 to map slabs from tomography, inferring a sinking rate, and assuming that slabs sink vertically.
761 Some limits to the approach are that slab sinking rates depend on depth because slabs slow
762 down as they approach the core-mantle boundary (Flament, 2019; Peng and Liu, 2022) and
763 that large-scale mantle flow may cause slabs to be advected laterally (Peng et al., 2021), which
764 is inconsistent with the assumption of vertically sinking slabs. The approach is also limited to
765 inferring past subduction zones from ~150 Ma and perhaps up to ~250 Ma depending on slab
766 sinking rates (Van der Meer et al., 2018; Flament, 2019). We note that this approach has been
767 used to infer the past location of subduction zones in some regions in the global tectonic
768 reconstructions that we use (e.g., Zahirovic et al., 2016). In this respect, our reconstructions of
769 past mantle flow are not entirely independent from tomographic models.
770
771 *4.2.3. Comparing slabs in global mantle flow and global tomographic models*
772 Comparisons between mantle flow and tomographic models have been carried out in
773 previous work (Bunge et al., 1998; Becker and Boschi, 2002), usually to derive global
774 correlations for both slow and fast structures. We map and quantify the spatial match between
775 mantle slabs and tomographic models down to 1,000 km depth, which complements previous
776 work that focused on the lower mantle (Flament, 2019) or on fewer tomographic models

(Shephard et al., 2012; Peng and Liu, 2023). Quantifying and visualising the match between slabs predicted by reconstructions of past mantle flow models and tomographic models makes it possible to identify areas where the models do not match tomographic models, so that tectonic reconstructions can be improved. This comparison (Fig. 6) suggests that global reference frames and the subduction history under north America (Liu et al., 2008), southern South America (Faccenna et al., 2017; Chen et al., 2019), between India and Asia (Zahirovic et al., 2012; Jagoutz et al., 2015) and under Japan (Domeier et al., 2017; Wu et al., 2022) may need to be refined in global tectonic reconstructions. In some locations, the timing or location of subduction zones is likely to be off in current global tectonic reconstructions. Improving tectonic reconstructions based on the match between mantle flow and tomographic models is complex and uncertain because the location of predicted slabs depends on the reference frame (Shephard et al., 2012) and on large-scale flow (Peng and Liu, 2023) which is determined by the assumptions and parameters of the flow model. Nevertheless, some first-order mismatches are intriguing. For example, global reconstructions show continuous subduction along South America for the last 500 Myr (Merdith et al., 2021), however, tomographic models suggest that subduction may have initiated around 50 Ma south of 38ºS (Faccenna et al., 2017; Chen et al., 2019). This problem requires further work, even though the resolution of tomographic models is limited in the southern hemisphere (Romanowicz, 2008).

The approach we used to assess the success of mantle flow models in matching slabs inferred from vote maps of tomographic model requires a strict match in the location of the predicted and inferred structure. This strict approach results in an overall relatively low sensitivity score (Fig. 7) because the target area is small (Fig. 1) and close matches (Fig. 6) are not considered. The approach could be improved to consider close matches for example by ‘stretching’ the models (Becker and Boschi, 2002) or by using an object-based approach as is done in weather forecasting (Davis et al., 2009). Another possible refinement of our method

802 would involve converting the predictions of our mantle flow models to seismic velocities and
803 filtering the results using a resolution operator (Schuberth et al., 2009; Shephard et al., 2012),
804 however, this would limit the comparison to tomographic models for which the resolution
805 operator is publicly available (Ritsema et al., 1999; Shephard et al., 2012).
806
807 **4. Conclusion**
808 We analysed the deep slab dip angles in paleo-geographically constrained mantle flow
809 models, and found that these models reproduce the first-order characteristics of penetrating
810 slabs (such as the Mariana Trench) and stagnating slabs (such as the Pacific slab to the north
811 of the Japanese Islands). Our results confirm that a key factor controlling deep slab dip angle
812 is the mobility of trenches, with stable trenches leading to slabs that penetrate into the lower
813 mantle, while retreating trenches can lead to slabs stagnating on top of the lower mantle. We
814 found that slabs can stagnate in the upper mantle if there is a viscosity contrast between the
815 upper mantle and the lower mantle, which is consistent with previous work. An increase in
816 viscosity by a factor of ten was sufficient to obtain slab stagnation in the considered models.
817 Our results suggest that deep slab dip angle can be used to calibrate the viscosity contrast
818 between the upper and lower mantle as well as the range of values for the Rayleigh number of
819 mantle flow models, because a small Rayleigh number (8.60×10^6) leads to stagnating slabs
820 globally, and a large Rayleigh number (8.60×10^9) leads to penetrating slabs globally. A
821 Rayleigh number equal to 8.60×10^8 was found to be appropriate for the considered models.
822 Our global models complement independent regional approaches and make it possible to
823 identify regions in which tectonic reconstructions should be revisited. For example, we suggest
824 that the retreat of the Pacific slab to the north of the Japanese Island could occur over a larger
825 distance and a longer period than in the reconstructions used in this work, and that the
826 subduction history along South America should be revisited before ~50 Ma and south of ~38ºS.

5. Acknowledgments

NF was supported by Australian Research Council grant LP170100863 (industry partner: De Beers). This research was undertaken with the assistance of resources from the National Computational Infrastructure (NCI), which is supported by the Australian Government. Access to NCI was partly supported by resources and services from the University of Wollongong (UOW). We thank Grace Shephard for comments that significantly improved this work. Figures 1, 3, 4, 6, 8-17 were prepared using GMT6 (Wessel et al., 2019), and Figures 5 and 7 were prepared using Matplotlib (Hunter, 2007). Data used in this work are available at https://zenodo.org/record/8251101.

6. Author contributions (CRediT author statement)

Joshua Weber: Formal Analysis, Investigation, Validation, Writing – Original Draft, Visualization. **Nicolas Flament:** Conceptualization, Methodology, Validation, Writing – Review & Editing, Visualization, Resources, Supervision, Project Administration, Funding Acquisition.

7. References

Agrusta, R., Goes, S. and Van Hunen, J., 2017. Subducting-slab transition-zone interaction: Stagnation, penetration and mode switches. Earth and Planetary Science Letters, 464: 10-23.

Amaru, M., 2007. Global travel time tomography with 3-D reference models, 274. Utrecht University.

Auer, L., Boschi, L., Becker, T., Nissen-Meyer, T. and Giardini, D., 2014. Savani: A variable resolution whole-mantle model of anisotropic shear velocity variations based on multiple data sets. Journal of Geophysical Research: Solid Earth, 119(4): 3006-3034.

Becker, T.W. and Boschi, L., 2002. A comparison of tomographic and geodynamic mantle models. Geochemistry, Geophysics, Geosystems, 3(1).

Běhounková, M. and Čížková, H., 2008. Long-wavelength character of subducted slabs in the lower mantle. Earth and Planetary Science Letters, 275(1-2): 43-53.

Billen, M.I., 2008. Modeling the dynamics of subducting slabs. Annual Review of Earth and Planetary Sciences, 36(1): 325-356.

Bower, D.J., Gurnis, M. and Flament, N., 2015. Assimilating lithosphere and slab history in 4-D Earth models. Physics of the Earth and Planetary Interiors, 238: 8-22.

860 Bunge, H.-P., Richards, M.A., Lithgow-Bertelloni, C., Baumgardner, J.R., Grand, S.P. and
861 Romanowicz, B.A., 1998. Time scales and heterogeneous structure in geodynamic
862 Earth models. Science, 280(5360): 91-95.
863 Burdick, S., van der Hilst, R.D., Vernon, F.L., Martynov, V., Cox, T., Eakins, J., Karasu,
864 G.H., Tylell, J., Astiz, L. and Pavlis, G.L., 2012. Model update March 2011: Upper
865 mantle heterogeneity beneath North America from traveltime tomography with global
866 and USArray Transportable Array data. Seismological Research Letters, 83(1): 23-28.
867 Burdick, S., Vernon, F.L., Martynov, V., Eakins, J., Cox, T., Tytell, J., Mulder, T., White,
868 M.C., Astiz, L. and Pavlis, G.L., 2017. Model update May 2016: Upper-mantle
869 heterogeneity beneath North America from travel-time tomography with global and
870 USArray data. Seismological Research Letters, 88(2A): 319-325.
871 Chang, S.J., Ferreira, A.M., Ritsema, J., van Heijst, H.J. and Woodhouse, J.H., 2015. Joint
872 inversion for global isotropic and radially anisotropic mantle structure including
873 crustal thickness perturbations. Journal of Geophysical Research: Solid Earth, 120(6):
874 4278-4300.
875 Chen, Y.-W., Wu, J. and Suppe, J., 2019. Southward propagation of Nazca subduction along
876 the Andes. Nature, 565(7740): 441-447.
877 Chopelas, A. and Boehler, R., 1992. Thermal expansivity in the lower mantle. Geophysical
878 Research Letters, 19(19): 1983-1986.
879 Christensen, U.R., 1996. The influence of trench migration on slab penetration into the lower
880 mantle. Earth and Planetary Science Letters, 140(1-4): 27-39.
881 Čížková, H. and Bina, C.R., 2019. Linked influences on slab stagnation: Interplay between
882 lower mantle viscosity structure, phase transitions, and plate coupling. Earth and
883 Planetary Science Letters, 509: 88-99.
884 Čižková, H. and Čadek, O., 1997. Effect of a Viscosity Interface at 1000 km Depth on
885 Mantle Circulation. Studia Geophysica et Geodaetica, 41(3): 297-306.
886 Čížková, H., van Hunen, J., van den Berg, A.P. and Vlaar, N.J., 2002. The influence of
887 rheological weakening and yield stress on the interaction of slabs with the 670 km
888 discontinuity. Earth and Planetary Science Letters, 199(3-4): 447-457.
889 Coltice, N., Husson, L., Faccenna, C. and Arnould, M., 2019. What drives tectonic plates?
890 Science advances, 5(10): eaax4295.
891 Coltice, N. and Shephard, G.E., 2018. Tectonic predictions with mantle convection models.
892 Geophysical Journal International, 213(1): 16-29.
893 Davis, C.A., Brown, B.G., Bullock, R. and Halley-Gotway, J., 2009. The method for object-
894 based diagnostic evaluation (MODE) applied to numerical forecasts from the 2005
895 NSSL/SPC Spring Program. Weather and Forecasting, 24(5): 1252-1267.
896 Domeier, M., 2016. A plate tectonic scenario for the Iapetus and Rheic oceans. Gondwana
897 Research, 36: 275-295.
898 Domeier, M., 2018. Early Paleozoic tectonics of Asia: Towards a full-plate model.
899 Geoscience Frontiers, 9(3): 789-862.
900 Domeier, M., Shephard, G.E., Jakob, J., Gaina, C., Doubrovine, P.V. and Torsvik, T.H.,
901 2017. Intraoceanic subduction spanned the Pacific in the Late Cretaceous–Paleocene.
902 Science Advances, 3(11): eaao2303.
903 Domeier, M. and Torsvik, T.H., 2014. Plate tectonics in the late Paleozoic. Geoscience
904 Frontiers, 5(3): 303-350.
905 Durand, S., Debayle, E., Ricard, Y. and Lambotte, S., 2016. Seismic evidence for a change in
906 the large-scale tomographic pattern across the D″ layer. Geophysical Research
907 Letters, 43(15): 7928-7936.

908 Durand, S., Debayle, E., Ricard, Y., Zaroli, C. and Lambotte, S., 2017. Confirmation of a
909 change in the global shear velocity pattern at around 1000 km depth. Geophysical
910 Journal International, 211(3): 1628-1639.
911 Dziewonski, A.M. and Anderson, D.L., 1981. Preliminary reference Earth model. Physics of
912 the Earth and Planetary Interiors, 25(4): 297-356.
913 Faccenna, C., Oncken, O., Holt, A.F. and Becker, T.W., 2017. Initiation of the Andean
914 orogeny by lower mantle subduction. Earth and Planetary Science Letters, 463: 189-
915 201.
916 Flament, N., 2019. Present-day dynamic topography and lower-mantle structure from
917 palaeogeographically constrained mantle flow models. Geophysical Journal
918 International, 216(3): 2158-2182.
919 Flament, N., Bodur, Ö.F., Williams, S.E. and Merdith, A.S., 2022. Assembly of the basal
920 mantle structure beneath Africa. Nature, 603(7903): 846-851.
921 French, S. and Romanowicz, B.A., 2014. Whole-mantle radially anisotropic shear velocity
922 structure from spectral-element waveform tomography. Geophysical Journal
923 International, 199(3): 1303-1327.
924 Fukao, Y. and Obayashi, M., 2013. Subducted slabs stagnant above, penetrating through, and
925 trapped below the 660 km discontinuity. Journal of Geophysical Research: Solid
926 Earth, 118(11): 5920-5938.
927 Fukao, Y., Widiyantoro, S. and Obayashi, M., 2001. Stagnant slabs in the upper and lower
928 mantle transition region. Reviews of Geophysics, 39(3): 291-323.
929 Garel, F., Goes, S., Davies, D., Davies, J.H., Kramer, S.C. and Wilson, C.R., 2014.
930 Interaction of subducted slabs with the mantle transition-zone: A regime diagram
931 from 2-D thermo-mechanical models with a mobile trench and an overriding plate.
932 Geochemistry, Geophysics, Geosystems, 15(5): 1739-1765.
933 Goes, S., Agrusta, R., van Hunen, J. and Garel, F., 2017. Subduction-transition zone
934 interaction: A review. Geosphere, 13(3): 644-664.
935 Goes, S., Capitanio, F.A. and Morra, G., 2008. Evidence of lower-mantle slab penetration
936 phases in plate motions. Nature, 451(7181): 981-984.
937 Grand, S.P., 2002. Mantle shear–wave tomography and the fate of subducted slabs.
938 Philosophical Transactions of the Royal Society of London. Series A: Mathematical,
939 Physical and Engineering Sciences, 360(1800): 2475-2491.
940 Griffiths, R.W., Hackney, R.I. and van der Hilst, R.D., 1995. A laboratory investigation of
941 effects of trench migration on the descent of subducted slabs. Earth and Planetary
942 Science Letters, 133(1-2): 1-17.
943 Guillou-Frottier, L., Buttles, J. and Olson, P., 1995. Laboratory experiments on the structure
944 of subducted lithosphere. Earth and Planetary Science Letters, 133(1-2): 19-34.
945 Hager, B. and Richards, M., 1989. Long-wavelength variations in Earth's geoid: physical
946 models and dynamical implications. Philosophical Transactions of the Royal Society
947 of London. Series A, Mathematical and Physical Sciences, 328(1599): 309-327.
948 Hager, B.H., Clayton, R.W., Richards, M.A., Comer, R.P. and Dziewonski, A.M., 1985.
949 Lower mantle heterogeneity, dynamic topography and the geoid. Nature, 313(6003):
950 541-545.
951 Honda, S., 2016. Slab stagnation and detachment under northeast China. Tectonophysics,
952 671: 127-138.
953 Hosseini, K., Matthews, K.J., Sigloch, K., Shephard, G.E., Domeier, M. and Tsekhmistrenko,
954 M., 2018. SubMachine: Web-based tools for exploring seismic tomography and other
955 models of Earth's deep interior. Geochemistry, Geophysics, Geosystems, 19(5): 1464-
956 1483.

Hosseini, K., Sigloch, K., Tsekhmistrenko, M., Zaheri, A., Nissen-Meyer, T. and Igel, H., 2020. Global mantle structure from multifrequency tomography using P, PP and P-diffracted waves. Geophysical Journal International, 220(1): 96-141.

Hosseini, K.M., Kara; Tsekhmistrenko, Maria, 2018. SubMachine; earth.ox.ac.uk/~smachine/cgi/index.php?page=vote_maps.

Houser, C., Masters, G., Shearer, P. and Laske, G., 2008. Shear and compressional velocity models of the mantle from cluster analysis of long-period waveforms. Geophysical Journal International, 174(1): 195-212.

Hu, J., Liu, L. and Zhou, Q., 2018. Reproducing past subduction and mantle flow using high-resolution global convection models. Earth and Planetary Physics, 2(3): 189-207.

Hunter, J.D., 2007. Matplotlib: A 2D graphics environment. Computing in science & engineering, 9(03): 90-95.

Irifune, T. and Ringwood, A., 1993. Phase transformations in subducted oceanic crust and buoyancy relationships at depths of 600–800 km in the mantle. Earth and Planetary Science Letters, 117(1-2): 101-110.

Jagoutz, O., Royden, L., Holt, A.F. and Becker, T.W., 2015. Anomalously fast convergence of India and Eurasia caused by double subduction. Nature Geoscience, 8(6): 475-478.

Jaxybulatov, K., Koulakov, I. and Dobretsov, N., 2013. Segmentation of the Izu-Bonin and Mariana slabs based on the analysis of the Benioff seismicity distribution and regional tomography results. Solid Earth, 4(1): 59-73.

Kido, M. and Čadek, O., 1997. Inferences of viscosity from the oceanic geoid: Indication of a low viscosity zone below the 660-km discontinuity. Earth and Planetary Science Letters, 151(3-4): 125-137.

King, S.D., 2016. An evolving view of transition zone and midmantle viscosity. Geochemistry, Geophysics, Geosystems, 17(3): 1234-1237.

Koelemeijer, P., Ritsema, J., Deuss, A. and Van Heijst, H.-J., 2016. SP12RTS: a degree-12 model of shear-and compressional-wave velocity for Earth's mantle. Geophysical Journal International, 204(2): 1024-1039.

Lekic, V., Cottaar, S., Dziewonski, A. and Romanowicz, B., 2012. Cluster analysis of global lower mantle tomography: A new class of structure and implications for chemical heterogeneity. Earth and Planetary Science Letters, 357: 68-77.

Lekić, V. and Romanowicz, B., 2011. Inferring upper-mantle structure by full waveform tomography with the spectral element method. Geophysical Journal International, 185(2): 799-831.

Li, C., van der Hilst, R.D., Engdahl, E.R. and Burdick, S., 2008. A new global model for P wave speed variations in Earth's mantle. Geochemistry, Geophysics, Geosystems, 9(5).

Liu, L., Spasojevic, S. and Gurnis, M., 2008. Reconstructing Farallon plate subduction beneath North America back to the Late Cretaceous. Science, 322(5903): 934-938.

Lu, C. and Grand, S.P., 2016. The effect of subducting slabs in global shear wave tomography. Geophysical Journal International, 205(2): 1074-1085.

Lu, C., Grand, S.P., Lai, H. and Garnero, E.J., 2019. TX2019slab: A new P and S tomography model incorporating subducting slabs. Journal of Geophysical Research: Solid Earth, 124(11): 11549-11567.

Ma, P., Liu, S., Gurnis, M. and Zhang, B., 2019. Slab horizontal subduction and slab tearing beneath East Asia. Geophysical Research Letters, 46(10): 5161-5169.

Mao, W. and Zhong, S., 2018. Slab stagnation due to a reduced viscosity layer beneath the mantle transition zone. Nature Geoscience, 11(11): 876-881.

Matthews, K.J., Maloney, K.T., Zahirovic, S., Williams, S.E., Seton, M. and Mueller, R.D., 2016. Global plate boundary evolution and kinematics since the late Paleozoic. Global and Planetary Change, 146: 226-250.

Merdith, A.S., Collins, A.S., Williams, S.E., Pisarevsky, S., Foden, J.D., Archibald, D.B., Blades, M.L., Alessio, B.L., Armistead, S. and Plavsa, D., 2017. A full-plate global reconstruction of the Neoproterozoic. Gondwana Research, 50: 84-134.

Merdith, A.S., Williams, S.E., Collins, A.S., Tetley, M.G., Mulder, J.A., Blades, M.L., Young, A., Armistead, S.E., Cannon, J. and Zahirovic, S., 2021. Extending full-plate tectonic models into deep time: Linking the Neoproterozoic and the Phanerozoic. Earth-Science Reviews, 214: 103477.

Montelli, R., Nolet, G., Dahlen, F. and Masters, G., 2006. A catalogue of deep mantle plumes: New results from finite-frequency tomography. Geochemistry, Geophysics, Geosystems, 7(11).

Moulik, P. and Ekström, G., 2014. An anisotropic shear velocity model of the Earth's mantle using normal modes, body waves, surface waves and long-period waveforms. Geophysical Journal International, 199(3): 1713-1738.

Müller, R.D., Seton, M., Zahirovic, S., Williams, S.E., Matthews, K.J., Wright, N.M., Shephard, G.E., Maloney, K.T., Barnett-Moore, N. and Hosseinpour, M., 2016. Ocean basin evolution and global-scale plate reorganization events since Pangea breakup. Annual Review of Earth and Planetary Sciences, 44(1): 107-138.

Müller, R.D., Zahirovic, S., Williams, S.E., Cannon, J., Seton, M., Bower, D.J., Tetley, M.G., Heine, C., Le Breton, E. and Liu, S., 2019. A global plate model including lithospheric deformation along major rifts and orogens since the Triassic. Tectonics, 38(6): 1884-1907.

Obayashi, M., Yoshimitsu, J., Nolet, G., Fukao, Y., Shiobara, H., Sugioka, H., Miyamachi, H. and Gao, Y., 2013. Finite frequency whole mantle P wave tomography: Improvement of subducted slab images. Geophysical Research Letters, 40(21): 5652-5657.

Olbertz, D., Wortel, M. and Hansen, U., 1997. Trench migration and subduction zone geometry. Geophysical Research Letters, 24(3): 221-224.

Panning, M., Lekić, V. and Romanowicz, B., 2010. Importance of crustal corrections in the development of a new global model of radial anisotropy. Journal of Geophysical Research: Solid Earth, 115(B12).

Peltier, W.R., 1996. Mantle viscosity and ice-age ice sheet topography. Science, 273(5280): 1359-1364.

Peng, D. and Liu, L., 2022. Quantifying slab sinking rates using global geodynamic models with data-assimilation. Earth-Science Reviews, 230: 104039.

Peng, D. and Liu, L., 2023. Importance of global spherical geometry to model slab dynamics and evolution in models with data assimilation. Earth-Science Reviews: 104414.

Peng, D., Liu, L., Hu, J., Li, S. and Liu, Y., 2021. Formation of East Asian Stagnant Slabs Due To a Pressure-Driven Cenozoic Mantle Wind Following Mesozoic Subduction. Geophysical Research Letters, 48(18): e2021GL094638.

Ren, Y., Stutzmann, E., van Der Hilst, R.D. and Besse, J., 2007. Understanding seismic heterogeneities in the lower mantle beneath the Americas from seismic tomography and plate tectonic history. Journal of Geophysical Research: Solid Earth, 112(B1).

Ricard, Y., Doglioni, C. and Sabadini, R., 1991. Differential rotation between lithosphere and mantle: a consequence of lateral mantle viscosity variations. Journal of Geophysical Research: Solid Earth, 96(B5): 8407-8415.

1053 Ricard, Y., Richards, M., Lithgow-Bertelloni, C. and Le Stunff, Y., 1993. A Geodynamic
1054 Model of Mantle Density Heterogeneity. Journal of Geophysical Research, 98(B12):
1055 21895-21,909.
1056 Ritsema, J., Deuss, A., Van Heijst, H. and Woodhouse, J., 2011. S40RTS: a degree-40 shear-
1057 velocity model for the mantle from new Rayleigh wave dispersion, teleseismic
1058 traveltime and normal-mode splitting function measurements. Geophysical Journal
1059 International, 184(3): 1223-1236.
1060 Ritsema, J., Heijst, H.J.v. and Woodhouse, J.H., 1999. Complex shear wave velocity
1061 structure imaged beneath Africa and Iceland. Science, 286(5446): 1925-1928.
1062 Ritsema, J., van Heijst, H.J. and Woodhouse, J.H., 2004. Global transition zone tomography.
1063 Journal of Geophysical Research: Solid Earth, 109(B2).
1064 Romanowicz, B., 2008. Using seismic waves to image Earth's internal structure. Nature,
1065 451(7176): 266-268.
1066 Rudolph, M.L. and Zhong, S., 2014. History and dynamics of net rotation of the mantle and
1067 lithosphere. Geochemistry, Geophysics, Geosystems, 15(9): 3645-3657.
1068 Schellart, W.P., 2007. The potential influence of subduction zone polarity on overriding plate
1069 deformation, trench migration and slab dip angle. Tectonophysics, 445(3-4): 363-372.
1070 Schuberth, B.S., Bunge, H.P. and Ritsema, J., 2009. Tomographic filtering of high-resolution
1071 mantle circulation models: Can seismic heterogeneity be explained by temperature
1072 alone? Geochemistry, Geophysics, Geosystems, 10(5).
1073 Searle, M.P. and Cox, J., 2002. Subduction zone metamorphism during formation and
1074 emplacement of the Semail ophiolite in the Oman Mountains. Geological Magazine,
1075 139(3): 241-255.
1076 Shephard, G.E., Bunge, H.-P., Schuberth, B.S., Müller, R., Talsma, A., Moder, C. and
1077 Landgrebe, T., 2012. Testing absolute plate reference frames and the implications for
1078 the generation of geodynamic mantle heterogeneity structure. Earth and Planetary
1079 Science Letters, 317: 204-217.
1080 Shephard, G.E., Houser, C., Hernlund, J.W., Valencia-Cardona, J.J., Trønnes, R.G. and
1081 Wentzcovitch, R.M., 2021. Seismological expression of the iron spin crossover in
1082 ferropericlase in the Earth's lower mantle. Nature Communications, 12(1): 5905.
1083 Shephard, G.E., Matthews, K.J., Hosseini, K. and Domeier, M., 2017. On the consistency of
1084 seismically imaged lower mantle slabs. Scientific reports, 7(1): 1-17.
1085 Simmons, N.A., Forte, A.M., Boschi, L. and Grand, S.P., 2010. GyPSuM: A joint
1086 tomographic model of mantle density and seismic wave speeds. Journal of
1087 Geophysical Research: Solid Earth, 115(B12).
1088 Simmons, N.A., Myers, S.C., Johannesson, G. and Matzel, E., 2012. LLNL-G3Dv3: Global P
1089 wave tomography model for improved regional and teleseismic travel time prediction.
1090 Journal of Geophysical Research: Solid Earth, 117(B10).
1091 Stadler, G., Gurnis, M., Burstedde, C., Wilcox, L.C., Alisic, L. and Ghattas, O., 2010. The
1092 dynamics of plate tectonics and mantle flow: From local to global scales. science,
1093 329(5995): 1033-1038.
1094 Steinberger, B. and Calderwood, A.R., 2006. Models of large-scale viscous flow in the
1095 Earth's mantle with constraints from mineral physics and surface observations.
1096 Geophysical Journal International, 167(3): 1461-1481.
1097 Steinberger, B. and Torsvik, T.H., 2008. Absolute plate motions and true polar wander in the
1098 absence of hotspot tracks. Nature, 452(7187): 620-623.
1099 Tesoniero, A., Auer, L., Boschi, L. and Cammarano, F., 2015. Hydration of marginal basins
1100 and compositional variations within the continental lithospheric mantle inferred from
1101 a new global model of shear and compressional velocity. Journal of Geophysical
1102 Research: Solid Earth, 120(11): 7789-7813.

Torsvik, T.H., Steinberger, B., Cocks, L.R.M. and Burke, K., 2008. Longitude: linking Earth's ancient surface to its deep interior. Earth and Planetary Science Letters, 276(3-4): 273-282.

Torsvik, T.H., Steinberger, B., Shephard, G.E., Doubrovine, P.V., Gaina, C., Domeier, M., Conrad, C.P. and Sager, W.W., 2019. Pacific-Panthalassic reconstructions: Overview, errata and the way forward. Geochemistry, Geophysics, Geosystems, 20(7): 3659-3689.

Torsvik, T.H., Van der Voo, R., Preeden, U., Mac Niocaill, C., Steinberger, B., Doubrovine, P.V., Van Hinsbergen, D.J., Domeier, M., Gaina, C. and Tohver, E., 2012. Phanerozoic polar wander, palaeogeography and dynamics. Earth-Science Reviews, 114(3-4): 325-368.

Torsvik, T.H. and Voo, R.V.d., 2002. Refining Gondwana and Pangea palaeogeography: estimates of Phanerozoic non-dipole (octupole) fields. Geophysical Journal International, 151(3): 771-794.

Trampert, J., Deschamps, F., Resovsky, J. and Yuen, D., 2004. Probabilistic tomography maps chemical heterogeneities throughout the lower mantle. Science, 306(5697): 853-856.

van der Hilst, R. and Mann, P., 1994. Tectonic implications of tomographic images of subducted lithosphere beneath northwestern South America. Geology, 22(5): 451-454.

van der Hilst, R. and Seno, T., 1993. Effects of relative plate motion on the deep structure and penetration depth of slabs below the Izu-Bonin and Mariana island arcs. Earth and Planetary Science Letters, 120(3-4): 395-407.

Van der Hilst, R.D., Widiyantoro, S. and Engdahl, E., 1997. Evidence for deep mantle circulation from global tomography. Nature, 386(6625): 578-584.

Van der Meer, D.G., Van Hinsbergen, D.J. and Spakman, W., 2018. Atlas of the underworld: Slab remnants in the mantle, their sinking history, and a new outlook on lower mantle viscosity. Tectonophysics, 723: 309-448.

Wessel, P., Luis, J., Uieda, L., Scharroo, R., Wobbe, F., Smith, W.H. and Tian, D., 2019. The generic mapping tools version 6. Geochemistry, Geophysics, Geosystems, 20(11): 5556-5564.

Williams, S., Wright, N.M., Cannon, J., Flament, N. and Müller, R.D., 2021. Reconstructing seafloor age distributions in lost ocean basins. Geoscience Frontiers, 12(2): 769-780.

Wu, J., Lin, Y.-A., Flament, N., Wu, J.T.-J. and Liu, Y., 2022. Northwest Pacific-Izanagi plate tectonics since Cretaceous times from western Pacific mantle structure. Earth and Planetary Science Letters, 583: 117445.

Wu, J., Suppe, J., Lu, R. and Kanda, R., 2016. Philippine Sea and East Asian plate tectonics since 52 Ma constrained by new subducted slab reconstruction methods. Journal of Geophysical Research: Solid Earth, 121(6): 4670-4741.

Yang, T., Moresi, L., Gurnis, M., Liu, S., Sandiford, D., Williams, S. and Capitanio, F.A., 2019. Contrasted East Asia and South America tectonics driven by deep mantle flow. Earth and Planetary Science Letters, 517: 106-116.

Young, A., Flament, N., Maloney, K., Williams, S., Matthews, K., Zahirovic, S. and Müller, R.D., 2019. Global kinematics of tectonic plates and subduction zones since the late Paleozoic Era. Geoscience Frontiers, 10(3): 989-1013.

Zahirovic, S., Matthews, K.J., Flament, N., Müller, R.D., Hill, K.C., Seton, M. and Gurnis, M., 2016. Tectonic evolution and deep mantle structure of the eastern Tethys since the latest Jurassic. Earth-Science Reviews, 162: 293-337.

Zahirovic, S., Müller, R.D., Seton, M., Flament, N., Gurnis, M. and Whittaker, J., 2012. Insights on the kinematics of the India-Eurasia collision from global geodynamic models. Geochemistry, Geophysics, Geosystems, 13(4).

1153